minerals

MDPI

Article

Characterization and Provenance of Carbonate Rocks for Quicklime and Dololime Production in Twin-Shaft Regenerative Kilns from the Arabian Peninsula and Neighboring Countries

Gabriele Vola [1,*], Matteo Ardit [2], Gianluca Frijia [2], Francesco Di Benedetto [2], Flavio Fornasier [3,4], Federico Lugli [5,6], Claudio Natali [7], Luca Sarandrea [1], Katharina Elena Schmitt [8] and Anna Cipriani [6]

1 Cimprogetti S.r.l., The Green Edge of Lime Technologies, 24044 Dalmine, Italy; l.sarandrea@cimprogetti.com
2 Department of Physics and Earth Sciences, University of Ferrara, 44122 Ferrara, Italy; matteo.ardit@unife.it (M.A.); gianluca.frijia@unife.it (G.F.); francesco.dibenedetto@unife.it (F.D.B.)
3 SOLIomics S.r.l., 33100 Udine, Italy; flavio@soliomics.com or flavio.fornasier@crea.gov.it
4 CREA—VE, 34170 Gorizia, Italy
5 Department of Cultural Heritage, University of Bologna (Campus of Ravenna), 48121 Ravenna, Italy; federico.lugli@unimore.it
6 Department of Chemical and Geological Sciences, University of Modena and Reggio Emilia, 41121 Modena, Italy; anna.cipriani@unimore.it
7 Department of Earth Sciences, University of Florence, 50121 Florence, Italy; claudio.natali@unifi.it
8 Institute of Geosciences, Johannes Gutenberg University, 55128 Mainz, Germany; katharina.schmitt@uni-mainz.de
* Correspondence: g.vola@cimprogetti.com or gabriele.vola@gmail.com

Abstract: This study analyzes high-grade carbonate rocks from several strategic deposits in the Arabian Peninsula and neighboring countries. The rocks are used locally for quicklime and dololime production in twin-shaft regenerative kilns. Stable C-O-Sr isotopes, along with chemical, mineralogical-petrographic analyses, micropaleontological investigations, cathodoluminescence microscopy, organic carbon speciation, and electron paramagnetic resonance spectroscopy, were used to trace the provenance of these rocks from economically significant non-metallic deposits. The resulting database can help identify and differentiate industrial raw materials that may appear similar chemically and/or macroscopically but have different textures/microstructures that can affect the properties of the derived burnt lime products. Various technological tests, including slaking reactivity, sticking tendency at high-temperature (i.e., 1300 °C), and physico-mechanical behavior of the lime, were performed to evaluate their suitability and predict lime performance in twin-shaft regenerative kilns. Comparison of laboratory and plant results validated the resulting database.

Keywords: high-grade carbonates; quicklime; dololime; industrial minerals characterization; twin-shaft regenerative kilns; Arabian Peninsula

check for updates

Citation: Vola, G.; Ardit, M.; Frijia, G.; Di Benedetto, F.; Fornasier, F.; Lugli, F.; Natali, C.; Sarandrea, L.; Schmitt, K.E.; Cipriani, A. Characterization and Provenance of Carbonate Rocks for Quicklime and Dololime Production in Twin-Shaft Regenerative Kilns from the Arabian Peninsula and Neighboring Countries. *Minerals* **2023**, *13*, 1500. https://doi.org/10.3390/min13121500

Academic Editor: Paulina Faria

Received: 25 September 2023
Revised: 15 November 2023
Accepted: 24 November 2023
Published: 29 November 2023

Copyright: © 2023 by the authors. Licensee MDPI, Basel, Switzerland. This article is an open access article distributed under the terms and conditions of the Creative Commons Attribution (CC BY) license (https://creativecommons.org/licenses/by/4.0/).

1. Introduction

Lime industry production starts by quarrying and crushing high-grade carbonate rocks sourced from carefully chosen deposits with well-defined geological features, logistical capabilities, volumetric availability, and physico-chemical properties [1]. Quicklime and dololime, the end products, are obtained by burning chemically "pure" limestones and dolostones at high temperatures in the range of 950–1350 °C [2,3].

Lime products with different properties and reactivities are required to satisfy different market segments [4–6]. The technical properties and reactivity of burnt lime products are significantly influenced by the physicochemical, mineralogical-petrographic, and textural-microstructural characteristics of carbonate rocks, as well as kiln technologies (static, rotary,

or regenerative), process parameters (residence time, heat consumption, combustion air), and fuel type (flame temperature) [7–11].

Given these stringent requirements for lime production, lime producers, such as steel manufacturers, typically avoid marly limestones and intermediate carbonates (such as dolomitic limestones and calcitic dolomites) in favor of pure endmembers (pure limestones and pure dolostones). However, marls and other clay-rich carbonates are useful in the production of natural hydraulic lime (NHL), the so-called "Roman" cement, which is mainly used for the preservation and restoration of cultural heritage [12,13]. Conversely, tectonically deformed or cataclastic/brecciated carbonates, as well as carbonate rocks that tend to be soily, dusty, or weak, such as chalk and medium- to coarse-grained marbles with low thermo-mechanical properties, are typically avoided as feedstocks for static and regenerative kilns due to the significant dust generation during production [11,14–17]. Otherwise, they can be successfully used in traditional rotary lime kilns, although this technology can be considered obsolete due to its high energy consumption and excessive emissions into the atmosphere. In fact, the entire lime industry is oriented towards greater environmental sustainability by constantly monitoring and improving the production process and minimizing greenhouse gas emissions (e.g., [18]).

As for lime technologies, a wide variety of kiln designs have been used over the years and around the world. Many alternatives with different costs are available for specific applications. Nowadays, parallel flow regenerative (PFR), also known as twin-shaft regenerative (TSR), is considered the best technology to achieve the target of soft-burnt reactive quicklime with different types of fuels [6]. TSR kilns have the lowest specific energy consumption compared to other types of kilns due to the regenerative process [19]. Indeed, TSR kilns represent the best compromise for reducing costs, gas emissions, and environmental impact [10].

The reactivity of quicklime plays a crucial role in steelmaking and a wide range of other industrial processes. These include chemical, pharmaceutical, mining, environmental, agricultural, soil and land stabilization, water and waste treatment, and food and beverage applications. Milk of lime is used for acid neutralization, while dry hydrated lime is used for flue gas desulfurization (FGD) [2,3]. It is worth emphasizing that double-hydrated dolomitic lime produced under pressure conditions is likely to have a significant impact on future generations of "green" sorbents. This is due to its potential porosimetric properties, which exceed those of traditional calcitic hydrated lime products [20].

Highly reactive dololime is considered one of the most powerful slagging agents for steelmaking [21]. Moreover, dolomite is suitable for a granular mixture of raw materials for the industrial glass-melting process [22]. Conversely, slow-reacting high-calcium lime is used in the casting of autoclaved aerated concretes [23]. Finally, dead-burnt or double-burnt dolomite is currently used in the production of magnesia refractories [24].

It follows that the correct choice of source rock has a fundamental economic impact on the lime industry. In addition, the performance of kilns and the quantity of lime required are determined by contractual obligations. It is therefore crucial to have strategic analytical procedures to trace the origin of raw materials and to use appropriate test methods for their technical characterization.

This study involved the analysis of 23 carbonates from different lime producers along the Arabian Gulf. The initial aim was to develop a comprehensive database that could be used to trace their provenance. A thorough characterization was also carried out to assess their suitability for use in TSR kilns. The multi-analytical approach used in this study was first applied in the field of archaeometry to determine the provenance of white marble artifacts for cultural heritage purposes [25–28].

The raw materials were subjected to a comprehensive analysis using various techniques, including geochemical-isotopic signature analysis, mineralogical-petrographic analyses, cathodoluminescence microscopy (CLM), electron paramagnetic resonance (EPR) spectroscopy, and carbon speciation. These analyses were complemented by slaking reac-

tivity and other technological tests, which helped to establish the required properties of the derived burnt lime products.

Finally, a comparison between laboratory and plant results was performed using a database obtained from a field campaign conducted in 2021 on a twin-shaft regenerative (TSR) kiln installed in Kuwait since 2009. This cross-checking process served to validate the reference database.

2. Geological Setting

The Arabian Peninsula consists of two distinct geological regions. The western half of the peninsula (and extending into eastern Africa) is an ancient landmass or shield, composed mostly of igneous and metamorphic Precambrian rocks. The eastern half of the peninsula is mostly sedimentary limestone, deposited in layers by expanding and receding ancient seas. These sedimentary layers were then gently folded by tectonic pressure from the east, resulting in the formation of the Zagros Mountains in Iran and Iraq. A geological sketch map of the area of interest showing the location of declared and identified source deposits used to feed TSR kilns is shown in Figure 1.

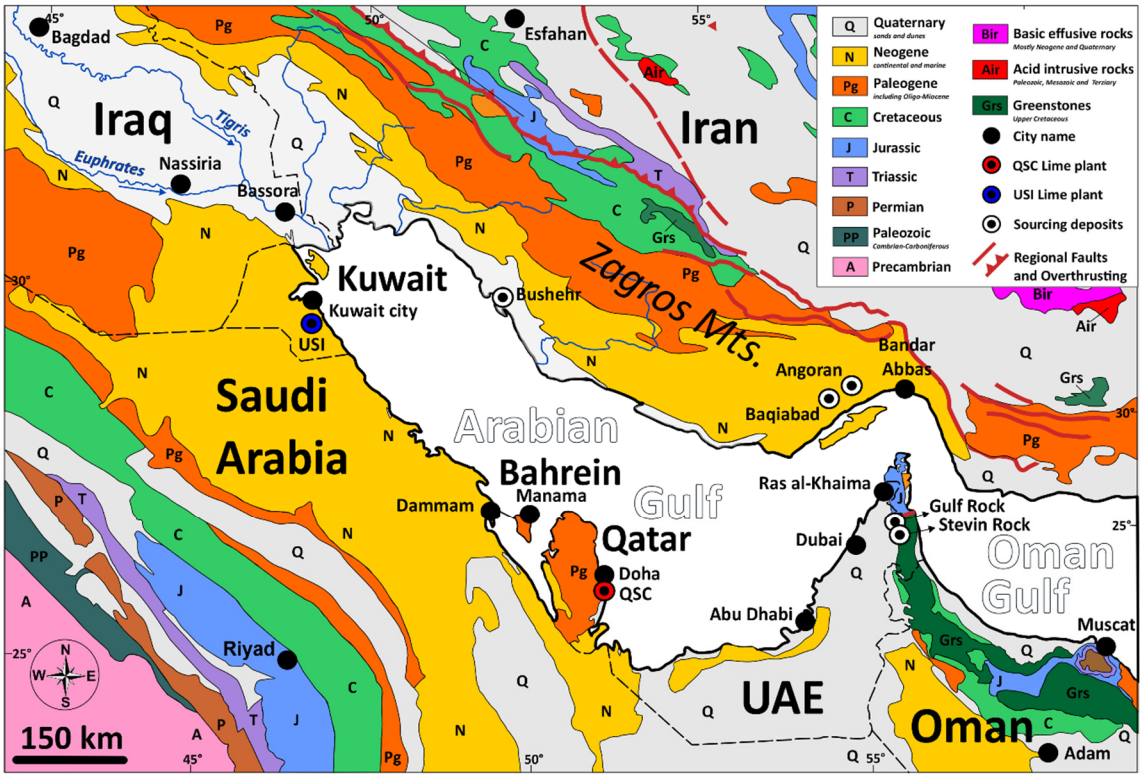


Figure 1. Geological sketch map of the Arabian Peninsula and neighboring countries (modified after ASGA–UNESCO, 1963) [29]. Location of Cimprogetti's lime plants and carbonate rock source deposits for feeding TSR kilns is also reported.

3. Materials and Methods

3.1. Sampling and Lithofacies Analysis

A total of 23 carbonate rocks were collected from various countries situated along the Persian Gulf, particularly Kuwait, Qatar, the United Arabian Emirates, and southern Iran. These rocks consisted of 15 limestones and 8 dolostones. Preliminary lithofacies studies were performed on rock fragments cut with a diamond wire. Colors were described using the Munsell rock-color chart [30]. Preliminary lithofacies description is given in Table 1.

Table 1. Preliminary lithological classification and declared provenance of carbonate rock samples from the Arabian Peninsula and neighboring countries. Colors according to the geological rock-color chart by Munsell [30]. Symbols legend: Lmt = limestone (no. 1–15); Dol = dolostone (no. 16–23), Nd = not declared.

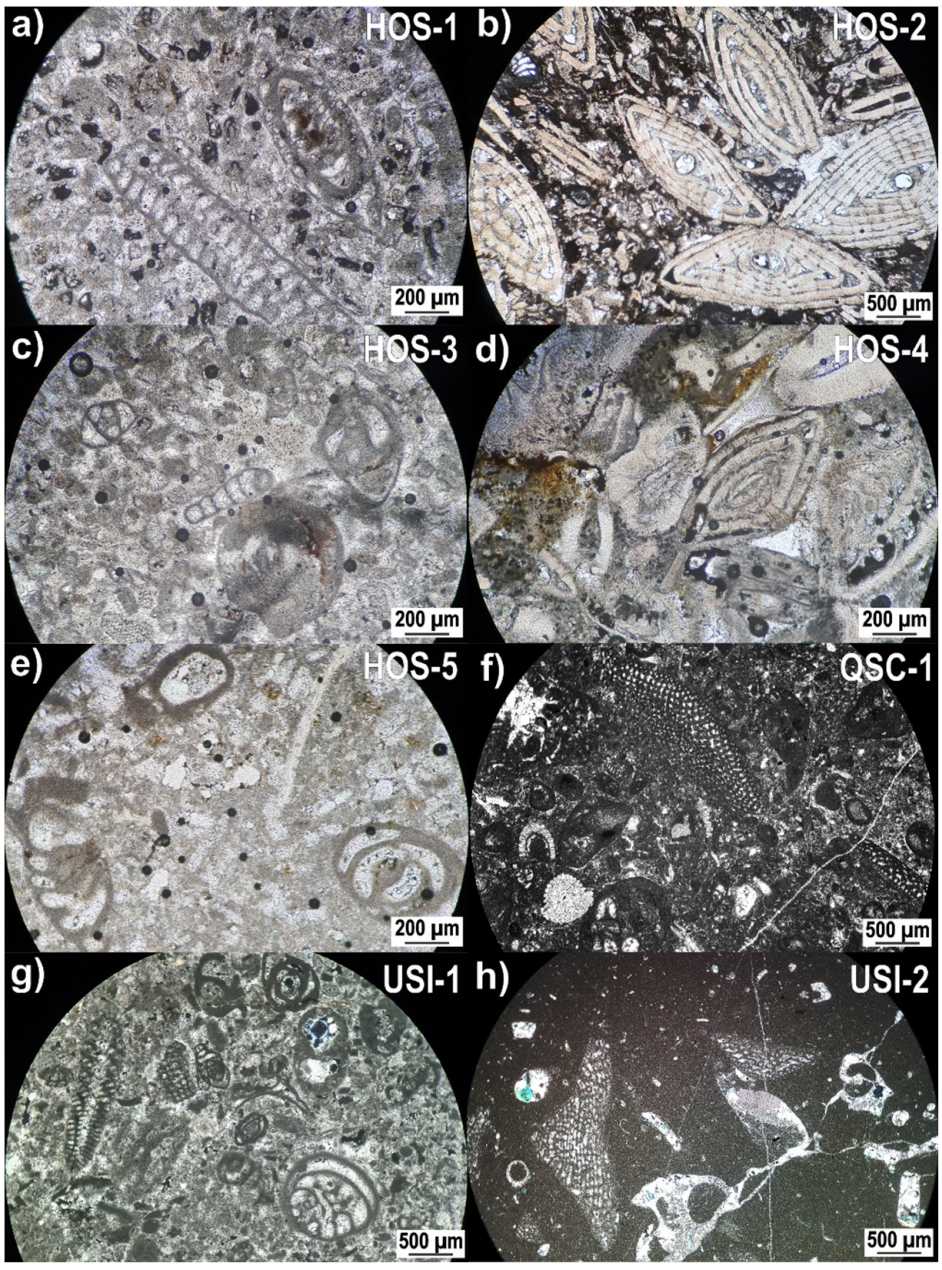
No.	Sample	Year	Type	Declared Provenance	Lithofacies	Primary Color	Subordinated Color
1	HOS-1	2014	Lmt	Mirzaei, Iran	Grain-supported texture	10 YR 8/6—yellow	5 YR—7/6 reddish yellow
2	HOS-2	2014	Lmt	Baqiabad, Iran	Grain-supported texture	10 YR 7/2—light gray	10 YR 7/6 yellow
3	HOS-3	2014	Lmt	Angoran, Iran	Grain-supported texture	7.5 YR 6/6 reddish yellow	-
4	HOS-4	2014	Lmt	Kashigari, Iran	Grain-supported texture	10 YR 7/4—very pale brown	10 YR 6/6 brownish yellow
5	HOS-5	2014	Lmt	Dargaz, Iran	Mud-to grain-supported texture	2.5 Y pale yellow	-
6	QSC-1	2014	Lmt	Nd	Mud-supported texture	10 YR 5/2 grayish brown	-
7	USI-1	2016	Lmt	Nd	Grain-supported texture	10 YR 8/1 white	10 YR 7/6 yellow
8	USI-2	2019	Lmt	Stevin Rock, UAE	Mud-supported texture	10 YR 4/1 dark gray	10 YR 4/2 dark grayish brown
9	USI-3	2019	Lmt	Gulf Rock, UAE	Grain-supported texture	2.5 Y 5/1 gray	2.5 Y 5/2 grayish brown
10	USI-4	2019	Lmt	UAE	Mud-supported texture	10 YR 7/3 very pale brown	10 YR 7/4 very pale brown
11	USI-5	2019	Lmt	Iran	Mud-to grain-supported texture	10 YR 7/3 very pale brown	10 YR 7/4 very pale brown
12	USI-6	2020	Lmt	Nd	Grain-supported texture	10 YR 5/1 gray	10 YR 4/1 dark gray
13	USI-7	2020	Lmt	Nd	Grain-supported texture	10 YR 7/1 light gray	10 YR 4/1 dark gray
14	USI-8	2021	Lmt	Jawhart, UAE	Grain-supported texture	10 YR 5/1 gray	-
15	USI-9	2022	Lmt	Stevin Rock, UAE	Mud-supported texture	10 YR 4/1 dark gray	10 YR 3/1 very dark gray
16	QSC-2	2014	Dol	Nd	Breccia-like texture	GLEY 1 7/7 light gray	-
17	USI-10	2016	Dol	Nd	Xeno-hypidiotopic mosaic	2.5 Y 7/1 light gray	2.5 Y 6/3 light yellowish brown
18	USI-11	2016	Dol	Stevin Rock, UAE	Breccia-like texture	2.5 Y 6/1 gray	2.5 Y 5/2 grayish brown
19	USI-12	2019	Dol	Bushehr, Iran	Hypidio- to porphyrotopic mosaic	2.5 Y 6/4 light yellowish brown	2.5 Y 5/3 light olive brown
20	USI-13	2020	Dol	Nd	Mud-supported (dolomitic)	2.5 Y 8/2 pale yellow	2.5 Y 7/3 pale yellow
21	USI-14	2020	Dol	Nd	Mud-supported (dolomitic)	10 YR 8/1 white	10 YR 7/2 light gray
22	USI-15	2020	Dol	Nd	Hypidio- to porphyrotopic mosaic	10 YR 7/3 very pale brown	10 YR 5/2 grayish brown
23	USI-16	2020	Dol	Nd	Hypidio- to porphyrotopic mosaic	10 YR 6/2 light brownish gray	10 YR 7/2 light gray

3.2. Carbonate Rocks and Burnt Limes Nomenclature

According to the geological literature, "limestone" and "dolostone" are sedimentary carbonate rocks with primary depositional textures and secondary diagenetic modifications [31–33]. The former has been classified according to [34–36]; the latter according to [37,38]. In this study, carbonate rocks were also defined on the basis of the impurity content, i.e., the so-called insoluble residue (IR), according to [11]. The terms "calcium lime" or "quicklime" and "dolomitic lime" or "dololime" indicate burnt products, i.e., air limes, derived from the calcination of limestone, and dolostone, respectively [39].

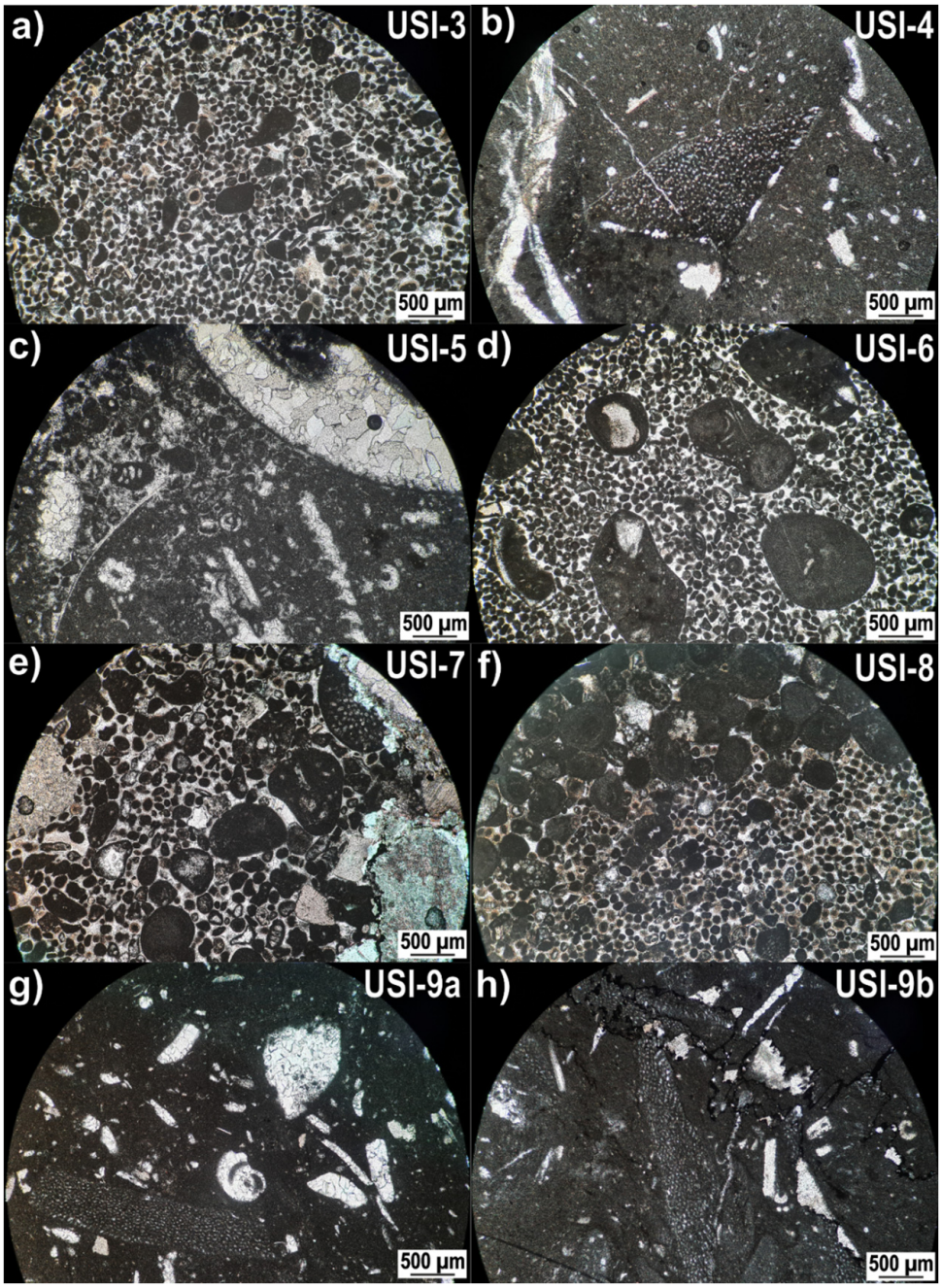
3.3. Petrographic Analysis and Cathodoluminescence Microscopy

Petrographic analysis was performed at Cimprogetti's laboratory on 100 thin sections using plane-polarized light microscopy (PLM) equipped with a high-resolution (4000 × 3000 pixels) digital camera (see Figure 2A–C). Alizarine-red staining was used to distinguish calcite from dolomite [40]. Moreover, 25 selected double-polished thin sections of dolostones were examined at the Department of Physics and Earth Sciences of the University of Ferrara using a CITL MK5 cold cathodoluminescence (CLM) optical microscope, operating at 12–15 kV and a beam current of 250 µA (see Figure 3).



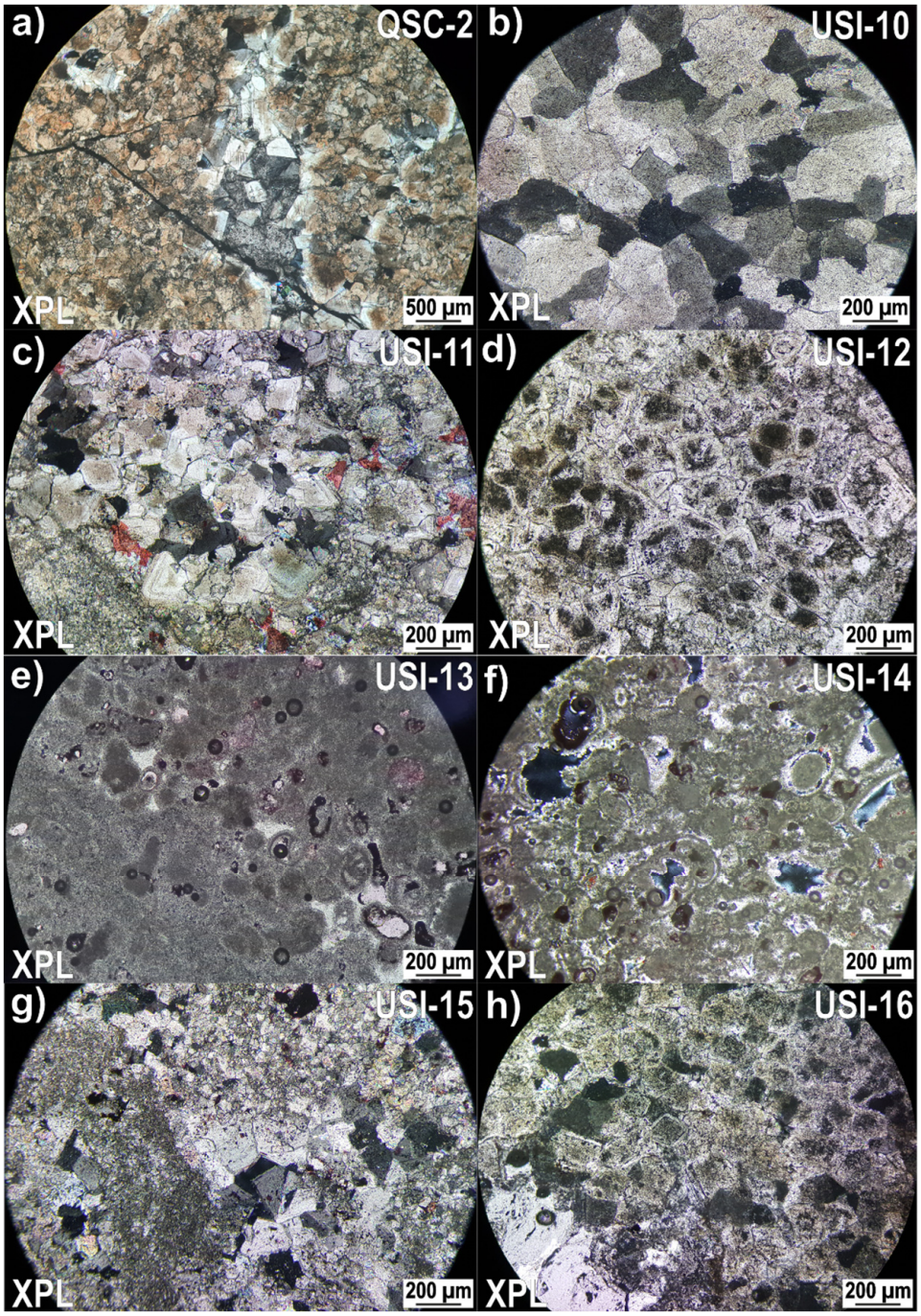
(A)

Figure 2. *Cont.*



(**B**)

Figure 2. *Cont*.



(**C**)

Figure 2. (**A**) Petrographic analysis of limestone samples (no. 1–8): (**a**) fossiliferous-peloidal wackestone to poorly sorted packstone with Miliolids forams from Mirzaei, Iran (microfacies 1, HOS-1); (**b**) porous poorly sorted packstone with large sub mm-sized Nummulites from Baqiabad, Iran (microfacies 1, HOS-2); (**c**) quite porous fossiliferous poorly sorted packstone with benthic forams from Angoran, Iran (microfacies 1, HOS-3); (**d**) quite porous poorly sorted packstone to grainstone with large mm-sized benthic foraminifera from Kashigari, Iran (microfacies 1, HOS-4); (**e**) porous fossiliferous wackestone to poorly sorted packstone with sporadic benthic forams from Dargaz, Iran (microfacies 2, HOS-5); (**f**) fossiliferous wackestone with benthic faunas, coated grains, and peloids. The dark micritic matrix is enriched in organic matter with quartz, clays, and pyrite. The source deposit can be traced back to Stevin Rock, UAE (microfacies 3, QSC-1); (**g**) porous and fossiliferous poorly sorted packstone with large benthic forams. The source deposit can be traced back to the unknown site no. 1 (microfacies 1, USI-1); (**h**) fossiliferous wackestone passing to poorly sorted

packstone with large mm-sized benthic fauna. Dark micritic carbon-rich matrix with clays and quartz. The provenance is from Stevin Rock, UAE (microfacies 3, USI-2). Micrographs taken under Plane-Polarized Light (PPL). (**B**) Petrographic analysis of limestone samples (no. 9–16): (**a**) Ooidal-peloidal grainstone, well-selected from the granulometric point of view, with benthic forams, coated grains, and lumps. The provenance is from Gulf Rock, UAE (microfacies 4, USI-3), (**b**) fossiliferous wackestone with benthic forams, and other bioclasts. The dark micritic matrix is enriched in organic carbon, and clays. The provenance is from Stevin Rock, UAE (microfacies 3, USI-4); (**c**) fossiliferous wackestone to poorly sorted packstone with large benthic forams, brachiopods, echinoids, and bivalvia. The dark matrix is composed of an organic carbon-rich micrite. The declared provenance is from Iran (microfacies 2, USI-5); (**d**) Peloidal-fossiliferous poorly sorted packstone to grainstone with large benthic fauna, coated grains, and lumps from Gulf Rock, UAE (microfacies 4, USI-6); (**e**) peloidal-fossiliferous poorly sorted packstone to grainstone with erosional surface and secondary chert replacements from Gulf Rock, UAE (microfacies 4, USI-7); (**f**) peloidal-fossiliferous poorly sorted packstone to grainstone with sporadic microfauna content from Jawhart Rock, UAE (microfacies 4, USI-8); (**g**,**h**) fossiliferous wackestone with mm-sized benthic forams and dark micritic matrix from Stevin Rock, UAE (microfacies 3, USI-9). Micrographs taken under Plane Polarized Light (PPL). (**C**) petrographic analysis of dolostone samples (no. 17–23): (**a**) dolostone with a breccia-like texture composed of non-planar xenotopic to planar euhedral idiotopic mosaic of brownish zoned dolomite crystals from Stevin Rock, UAE (microfacies 5, QSC-2); (**b**) hypidiotopic mosaic of fabric dolomite crystals with amoeboid boundary shape and high moldic intercrystalline porosity, laterally passing to xenotopic mosaic of brownish dolomite. The source deposit can be traced back to the unknown site no. 2 (microfacies 7, USI-10); (**c**) breccia-like texture composed of a planar euhedral hydiotopic mosaic of brownish and zoned dolomite crystals and a fine-grained matrix that isolates portions of parental rock, i.e., ghostly peloidal-fossiliferous limestone. The provenance is from Stevin Rock (microfacies 5, USI-11); (**d**) packed mosaic of hypidiotopic equigranular zoned crystals of dolomite with lobate boundary shape from Bushehr, Iran (microfacies 8, USI-12); (**e**,**f**) porous peloidal-fossiliferous dolomitic wackestone with benthic fauna, i.e., forams, gastropods, and bivalve microfossils. The source deposit can be traced back to the unknown site no. 3 (microfacies 6, USI-13 and USI-14); (**g**,**h**) equigranular hydiotopic-to-hypidiotopic mosaic of brownish rhombohedral dolomite crystals. The source deposit can be traced back to Bushehr, Iran (USI-15 and USI-16). Micrographs taken under Crossed Polarized Light (XPL).

3.4. Wavelength Dispersive X-ray Fluorescence Spectroscopy

Chemical analyses were carried out at Cimprogetti's laboratory using a combination of fusion bead and pressed powder methods. Whole-rock samples were ground in a stainless-steel vessel ring mill. An aliquot of each sample was dried at 105 °C and then fired at 1050 °C for 2 h to determine the loss on ignition (LOI). The powders were then mixed with an organic binder wax (9:1 ratio) and pelletized in 40 mm aluminum cups using a manual hydraulic press at 35 MPa for 1 min. Fusion beads were prepared by mixing 1 g of calcined lime powder with 10 g of lithium metaborate/tetraborate fusion flux (composition: 35.3 wt% Li tetraborate 64.7 wt% Li metaborate) using the Nieka E1 fluxer for XRF Sample Preparation (Quebec City, Canada). Chemical analyses were carried out using a Rigaku Supermini 200 wavelength dispersive X-ray fluorescence spectrometer (WD-XRF) (Osaka, Japan) with a Pd anode operating at 200 W. Calibration curves, based on 12 international standards of carbonate rocks, are linear for major, minor, and trace elements. Deviation values for repeatability tests are also very low [41].

3.5. Pre-Treatments for Insoluble Residues Extraction

The extraction of the insoluble residue from carbonate rocks was performed by a pre-treatment with 1 N hydrochloric acid for a maximum of 20 min [42]. This procedure minimizes the digestion of impurities such as clay minerals, especially illite/montmorillonite mixed layers [43].

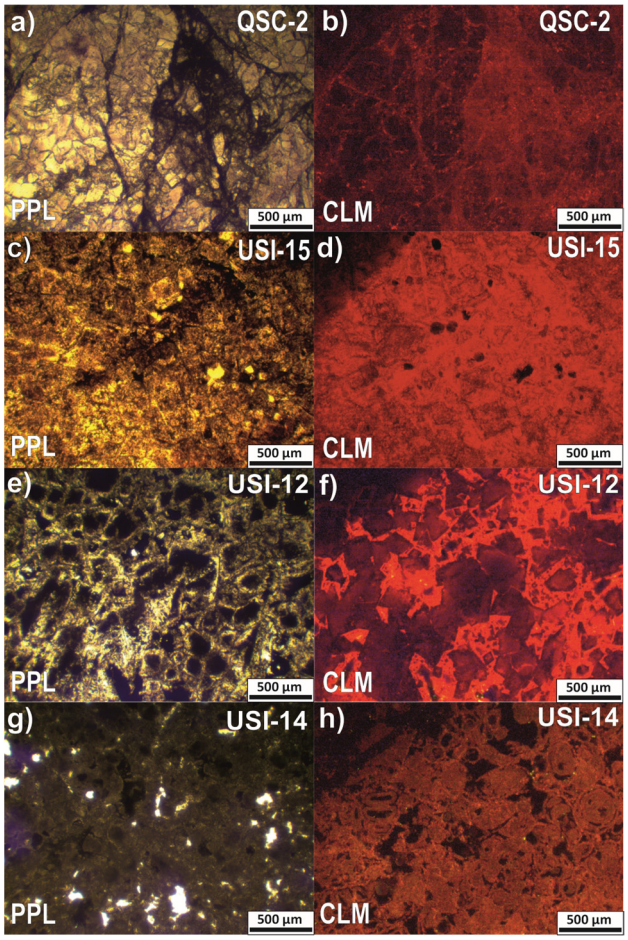


Figure 3. Plane-Polarized (PPL) and Cathodoluminescence Light Microphotographs (CLM) of main dolostone samples: (**a**,**b**) microfacies 5, Stevin Rock, UAE (QSC-2); (**c**,**d**) microfacies 8, Bushehr, Iran (USI-15); (**e**,**f**) microfacies 8, Bushehr, Iran (USI-12); (**g**,**h**) microfacies 6, unknown site no. 3 (USI-14).

3.6. X-ray Diffraction and Quantitative Phase Analyses

X-ray powder diffraction (XRPD) data collection was performed at Cimprogetti's laboratory using a Rigaku Miniflex 600 diffractometer (Tokio, Japan) operating in Bragg-Brentano geometry and equipped with a Rigaku D/teX ultra-high-speed detector (Tokio, Japan) set to discriminate the Cu$K\alpha_{1,2}$ radiation. The powder of each sample (i.e., whole rock and its insoluble residue) was side-loaded in a flat sample holder and scanned in the angular range 2.5–90 °2θ with a step size of 0.02 °2θ and a counting time of 0.4 s per step. Both identification and quantification of mineral phases were performed using the Rigaku PDXL2 software package (version no. 2.8.1.1). Quantitative phase analysis (QPA) was carried out by whole powder pattern fitting (WPPF) using the Rietveld method [44,45]. The lower detection limit (LDL) was significantly improved by recalculating the insoluble residue weight fraction on the whole rock samples.

3.7. Stable C-O and Sr Isotopes

Stable isotope ($\delta^{13}C$ and $\delta^{18}O$) analyses were performed at the University of Ferrara using an elemental isoprime precisION isotope ratio mass spectrometer with an integrated CentrION module in combination with an Elementar© isoFLOW headspace analyzer (Langenselbold, Germany) operated by the Elementar© ionOS® IRMS software version no. 5.0.4.118 (Cheadle, UK). Viscous anhydrous orthophosphoric acid (104%) was used to release the CO_2 from the carbonate samples. The reaction time was set to 7 h at 50 °C for dolomite samples and to 3 h at 50 °C. The in-house MAQ-1 standard was used for a one-point calibration. In addition, the measurement was monitored against two

control reference materials (IAEA 603 and IAEA CO-1). Analyses of the in-house standards performed on the analyzed samples give a precision of 0.07‰ for $\delta^{13}C$ and 0.08‰ for $\delta^{18}O$. The resulting values are reported in the conventional delta notation, relative to the Vienna-Pee Dee formation Belemnite (VPDB) international standard, in parts per million (‰). Mixed dolomite-calcite samples were analyzed twice. The first time as bulk material and the second time as pure dolomite after the removal of the calcite phase. Depending on the calcite/dolomite concentration (as determined by XRPD analyses), an aliquot of the sample (3 g) was treated with 10 mL of acetic acid at different times, as follows in Table 2.

Table 2. Acid treatment of dolomitic samples.

Dolomite Content (wt%)	Time of Acetic Acid Treatment (h)
70–90	1.5
50–70	2.0
30–50	3.0
<30	No further treatment

The test tubes containing the sample/acid mixture were shaken every 20 min so that the acid reached all the grains. After acidification, all samples were rinsed three times with distilled water and then dried overnight at 40 °C. The samples were then prepared for stable isotopic measurements.

The samples were also analyzed for Sr-isotopes at the Department of Chemical and Geological Sciences of the University of Modena and Reggio Emilia. They were prepared in a class 1000 clean laboratory under a class 10 laminar flow hood. 5–10 mg of powder was washed with MilliQ and digested with 6 M HNO_3. After drying, samples were redissolved in 3 M HNO_3 and centrifuged. They were then injected into Eichrom Sr spec-resin-filled columns, washed with 3 N HNO_3, and Sr was finally eluted with ultrapure MilliQ® water. The $^{87}Sr/^{86}Sr$ ratio was measured using a double-focusing MC-ICPMS with a forward Nier–Johnson geometry supplied by Thermo Fisher Scientific Neptune™ (Bremen, Germany), and the $^{87}Sr/^{86}Sr$ values obtained were corrected for baseline, mass bias, and interferences according to [46]. Finally, $^{87}Sr/^{86}Sr$ ratios were reported against the NIST SRM 987 value of 0.710248 [47]. Repeated analyses of the NIST SRM 987 yielded an average $^{87}Sr/^{86}Sr$ ratio of 0.710232 ± 0.000017 (2 SD, n = 5).

3.8. Carbon Speciation and Total Organic Carbon

Carbon speciation was refined at SOLIomics by an innovative method recently defined as "smart combustion" [48] using an Elementar SoliTOC analyzer (Langenselbold, Germany), which allows an oxidation-temperature-dependent differentiation of distinct carbon fractions. The analytical run takes approximately 1600 s and involves three steps of heating the samples to 400 °C, 600 °C, and 900 °C, with holding times of 230, 120, and 150 s, respectively. The CO_2 produced was detected by an infrared detector. Accuracy and precision, evaluated by repeated analyses of samples and of soil standards, were better than 5% of the measured concentration [49]. Analyses of TOC were divided into TOC400, i.e., the labile form destabilizing at temperatures below 400 °C, and ROC, i.e., the residual oxidizable carbon destabilizing at temperatures between 400 and 600 °C. See Supplementary Materials Table S1 for more information.

3.9. Electron Paramagnetic Resonance Spectroscopy

Samples were analyzed at the Chemistry Department of the University of Florence by placing an aliquot of the dry powder in amorphous silica tubes using bags prepared with conventional Teflon tape. The tubes were chosen to avoid the presence of transition metal impurities (mainly Fe or Cr) in the glassy matrix, which are likely to interfere with the EPR spectra of the samples. EPR spectral measurements were carried out at room temperature using a conventional Bruker ER 200D-SRC operating at ~9.5 GHz (X-band).

Spectra were recorded at 0.4 mT modulation amplitude and 100 KHz modulation frequency. The post-amplification gain setting was optimized to maximize the signal-to-noise ratio. All spectra were recorded in a magnetic field range of 300–380 mT, with a field step of 0.039 mT and a scan speed of 0.4 mT/s. See Supplementary Materials Table S2 and Figure S1 for more information.

3.10. Burning Tests

In order to simulate the firing conditions of a TSR kiln, crushed rock samples of 30–60 mm in size were burned using a muffle furnace under static air conditions. The standard procedure performed at Cimprogetti's laboratory consisted of 6-h burning trials, namely, 3 h of preheating followed by 3 h at the maximum temperature (T_{max}). Two different temperatures were used: a T_{max} of 1050 °C was chosen to simulate natural gas firing conditions, while a higher T_{max} of 1150 °C was used to represent solid fuel (i.e., coal and carbon coke) firing conditions. Limes obtained from these burning trials have a residual CO_2 content close to zero.

3.11. Mechanical Degradation and Drop Test

Lime pebbles obtained from the burning tests at 1050 °C were then subjected to mechanical degradation (MD) and drop tests (DT). These tests were carried out to simulate the process of lime decrepitation and to predict the formation of dust during the calcination process, as well as at the discharging drawers of the kiln [11,15–17]. Lumps of lime are therefore sieved for 10 min on a 10 mm sieve using an automatic device. The fine (<10 mm) and coarse (>10 mm) fractions were both weighed, and the coarse fraction (>10 mm) was also manually sieved on a >19 mm sieve. The >19 mm fraction was sealed in a plastic bag and then dropped 5 times from a height of 2 m. Finally, the sample was sieved again at a >19 mm sieve and weighed. MD and DT were calculated according to the following equations (Equations (1)–(3)).

$$\text{MD}(\%)\text{at 10 mm} = \frac{\text{sample weight (g)} < 10\text{ mm}}{\text{sample weight (g) before sieving}} \cdot 100 \quad (1)$$

$$\text{MD}(\%)\text{ at 19 mm} = \frac{\text{sample weight (g)} < 19\text{ mm}}{\text{sample weight (g) before sieving}} \cdot 100 \quad (2)$$

$$\text{DT}(\%) = \frac{\text{sample weight (g) after the DT} < 19\text{ mm}}{\text{sample weight (g) before the DT (g)}} \cdot 100 \quad (3)$$

3.12. Slaking Reactivity Tests

The reactivity tests were performed on quicklime and dololime samples obtained from the above-mentioned burning tests at 1050 and 1150 °C, according to the European test method [50]. 150 g of powdered lime is placed in a Dewar flask containing 600 mL of demineralized water at 20 °C; the milk of lime is kept in motion by a stirrer at a constant speed of 300 rpm. The following parameters are then measured: (1) the temperature rise, i.e., ΔT 40 °C (or t_{60}) for quicklime and ΔT 30 °C (or t_{50}) for dololime; (2) the maximum slaking temperature (T_{max}) and the total active slaking time (TAST). In practice, slaking reactivity is defined as follows: very high reactivity: t_{60}-t_{50} < 1 min; high reactivity: 1 < t_{60}-t_{50} < 3 min; medium reactivity: 3 < t_{60}-t_{50} < 6 min; low reactivity: t_{60}-t_{50} > 6 min.

3.13. Overburning Test Method and Sticking Tendency

The sticking tendency of the lime at high temperature (i.e., 1300 °C) was determined at Cimprogetti's laboratory according to the overburning test method (OBT) [11], which allows the evaluation of lime densification, agglomeration, and sporadic melting at the highest operating temperature of the kiln. For this purpose, 75 g of the granulated sample is placed in a quartz crucible at 1300 °C for 3 h. After the thermal treatment, the sample is weighed and classified according to the ST classification given in Table 3.

Table 3. Sticking Tendency (ST) classification based on block weight (g) from the Overburning Test (OBT) method integrated with guidelines for plant commissioning.

Symbol Color	Blocks Weight (g)	ST Group	Guidelines for Plant Commissioning	
			Recommended Size Fractions	Residua CO_2 Guarantee (%)
	Completely melted	A	No fraction recommended	Material is rejected
	Very-high (VH-ST: >20 g)	B	Coarse fraction warmly recommended + low lime mechanical degradation	No guarantee
	High (H-ST: 18–20 g)		Coarse fraction warmly recommended	5.0
	Medium high (MH-ST: 16–18 g)	C	A coarse fraction to feed the kiln is recommended	3.5
	Medium (M-ST: 14–16 g)			2.5
	Medium-Low (ML-ST: 12–14 g)			2.0
	Slight (S-ST: 10–12 g)	D	No specific requirements For raw materials	1.0
	Low (L-ST: <10 g)			1.0

The degree of ST (%) for a lime and a dololime block is calculated according to the following equations (Equations (4) and (5)):

$$\mathrm{ST}(\%) = \frac{\text{lime block weight (g)}}{42.0(\text{ g})} \cdot 100 \quad (4)$$

where 42 g is the weight of the lime as a whole if 75 g of pure limestone $CaCO_3$ completely converts into lime (CaO) at the end of the OBT. Analogously, for a dolomite aggregate (dololime):

$$\mathrm{ST}(\%) = \frac{\text{dololime block weight (g)}}{39.2\text{ (g)}} \cdot 100 \quad (5)$$

where 39.2 g is the weight of the dololime as a whole if 75 g of a pure dolomite $CaMg(CO_3)_2$ completely converts into dololime (58.2 wt.%·CaO + 41.8 wt.%·MgO) at the end of the OBT.

4. Results and Discussion

4.1. Integrated Microfacies Analysis

Samples were classified into eight different microfacies, including four types of limestone and four types of dolostone. This classification is based on main lithological features and colors, coupled with detailed mineralogical-petrographic analyses and fossiliferous content (Tables 4–6, Figure 2A–C). Moreover, cathodoluminescence microscopy allowed the identification of specific diagenetic features and typical cement stratigraphy of dolomitic samples, complementing the mineralogical-petrographic characterization (Figure 3). The above features are summarized as follows.

Table 4. (a). Petrographic analysis of limestone samples from the Arabian Peninsula and neighboring countries. Symbols legend: The question mark (?) indicates uncertainty regarding the determination of taxa and thus uncertainly about chronostratigraphic position of the source rock. (b). Petrographic analysis and cathodoluminescence microscopy of dolostone samples from the Arabian Peninsula and neighboring countries.

(a)

No.	Code	Sample	Main Depositional Features	Textural Components	Fossiliferous Content	Diagenetic Features	Estimated Age
1	1849	HOS-1	Peloidal-fossiliferous wackestone to poorly sorted packstone. Local accumulation of bioclasts (microfacies-1)	Dark micritic matrix enriched with organic carbon, goethite, and clay minerals, mostly illite	Large sub mm-sized benthic forams, i.e., *Orbitolites* sp., *Penarchaias glynnjonesi* sp. (Henson, 1950), Miliolids, Nummulites, plus bivalvia, bryozoan, echinoids, and crinoids	Several moldic porosities were filled in by microsparite and some veins were filled in by neomorphic mosaic of calcite cement	Eocene (Lutetian-Bartonian)
2	1850	HOS-2	Extremely porous, sporadically impure, peloidal-ooidal, and fossiliferous poorly sorted packstone (microfacies-1)	Oolithic-peloidal grainstone passing to a Nummulitic grainstone. Vuggy pores filled in by fibrous calcedony. Terrigenous quartz and feldspars extra-basinal grains plus some clay, mostly illite	Large sub mm-sized benthic forams, i.e., Nummulites, and Miliolidae	Early diagenetic dolomitization and fibrous calcedony fillings in vacuole and dissolution porosities	Eocene (Ypresian-Lutetian)
3	1851	HOS-3	Quite porous fossiliferous poorly sorted packstone with sporadic benthic foraminifera (microfacies-1)	Dark micritic matrix enriched with organic carbon, iron oxide-hydroxides, and clay minerals, mostly illite and chlorite	Large sub mm-sized forams, i.e., Orbitolites, Nummulites, *Neorhipidionina williamsoni*, Henson, 1948, *Peneroplis flabelliformis* Sirel & Özgen-Erdem in Sirel, Özgen-Erdem & Kangal, 2013, plus bivalvia, gastropods, bryozoa, echinoids and rare algae	Several vuggy porosities were filled in by microsparite, and some veins were filled in by neomorphic early diagenetic calcite cement.	Eocene (Bartonian-Priabonian)
4	1852	HOS-4	Quite porous poorly sorted packstone to grainstone with large mm-sized benthic foraminifera (microfacies-1)	Dark micritic matrix enriched of organic carbon and clay minerals, mostly illite, smectite, and palygorskite	Benthic forams, i.e., *Operculina*, *Amphistegina*, plus scleractinian corals, echinoids, bryozoan, brachiopods, and oyster fragments	Moldic porosity filled in by neomorphic calcite cement. Early diagenetic dolomitization	Oligocene/ Miocene
5	1853	HOS-5	Porous fossiliferous wackestone to poorly sorted packstone with sporadic benthic forams (microfacies-2)	Dark micritic matrix enriched of organic carbon, quartz, feldspars, and clay minerals, mostly illite and smectite	Benthic forams, i.e., *Nezzazzata* sp?, *Edomia reicheli*, *Multispira* sp.?, plus gastropods, bivalve, red algae, and bryozoan fragments	Vuggy cavities and moldic porosity are filled in by early diagenetic sparry calcite. Early diagenetic dolomitization	Upper Cretaceous (Late Cenomanian)
6	1880	QSC-1	Fossiliferous wackestone passing to poorly sorted packstone with benthic faunas, coated grains and peloids. (microfacies-3)	Dark micritic matrix enriched of organic carbon with quartz and clay mineral, mostly illite. Anoxic depositional conditions because the presence of pyrite within the insoluble residue.	Large sub mm-sized benthic forams, i.e., *Palorbitolina* sp., *Salpingoporella dinarica*, plus echinoids, crinoids, and brachiopods	Moldic porosity filled in by mosaic early diagenetic microsparite and/or mosaic calcite cement.	Lower Cretaceous (early Aptian)

Table 4. *Cont.*

No.	Code	Sample	Main Depositional Features	Textural Components	Fossiliferous Content	Diagenetic Features	Estimated Age
7	2306	USI-1	Porous and fossiliferous poorly sorted packstone with large benthic forams (microfacies-1)	Dark micritic matrix enriched of organic carbon and clay minerals, i.e., mostly illite and smectite, plus quartz and goethite	Large sub mm-sized benthic forams, i.e., *Neorhipidionina williamsoni,* Henson, 1948, *Coskinolina perpera* Hottinger & Drobne, *Omanodiscus teniussimus*, plus red algae, and brachiopods	Moldic porosity partially filled in by mosaic early diagenetic sparry-calcite cement	Eocene, Lutetian-Priabonian
8	3109	USI-2	Fossiliferous wackestone passing to poorly sorted packstone with large mm-sized benthic fauna (microfacies-3)	Dark micritic matrix enriched with organic carbon, illite, goethite, and quartz	Large mm-sized brachiopods, benthic forams, i.e., *Palorbitolinoides* sp., plus bivalvia, echinos, and gastropods	Sub mm-sized moldic and bioclastic porosity filled in by early diagenetic mosaic sparry-calcite. Sporadic stylolite joints.	Lower Cretaceous (upper Barremian-lower Aptian)
9	3110	USI-3	Ooidal-peloidal grainstone with benthic forams, lumps, and coated grains (microfacies-4)	Very thin ooids are very well selected from the granulometric point of view	Benthic Miliolid forams, i.e., *Vidalina radoicicae* sp., and echinoids	Early diagenetic sparry-calcite cement	Upper Cretaceous (middle/late Cenomanian?)
10	3127	USI-4	Fossiliferous wackestone with benthic forams, thin shell fragments and tiny bioclasts (microfacies-3)	Dark micritic matrix enriched with organic matter	Large sub mm-sized benthic forams, i.e., *Palorbitolina lenticularis*, plus echinoids, gastropods, thin shells, and tiny bioclasts	Early diagenetic sparry-calcite cement in some veins and sporadic moldic porosity	Lower Cretaceous (Aptian)
11	3210	USI-5	Fossiliferous wackestone to poorly sorted packstone (microfacies-2)	Dark micritic matrix enriched with organic matter	Both pelagic and benthonic fauna, i.e., calpionella, *Trocholina* sp., Miliolids, plus brachiopods, echinoids, and mm-sized bivalvia	Sporadic moldic porosity filled in by early diagenetic calcite cement.	Early-'mid'-Cretaceous
12	3222	USI-6	Peloidal and fossiliferous poorly sorted packstone to grainstone with large benthic microfossils and lumps (microfacies-4)	Very thin peloidal grains are very well selected from the granulometric point of view	Forams, i.e., *Bispiraloconulus* sp., echinos, and bivalvia	Some veins are filled in by neomorphic calcite cement. Sporadic chert replacements of calcite cement within some peloidal porosity	Lower Cretaceous (Berrasian/ Valanginian)
13	3352	USI-7	Peloidal and fossiliferous poorly sorted packstone to grainstone with large benthic fauna and lumps (microfacies-4)	Very thin peloidal grains are very well selected from the granulometric point of view.	Large mm-sized benthic fauna, including bryozoa, echinoids, and bivalvia, plus Cyanobacteria nodule (cayeuxa like)?	Some erosional surfaces with dissolution and early diagenetic microcrystalline chert replacements. Veins with early diagenetic calcite cement.	Lower Cretaceous?
14	3581	USI-8	Peloidal and fossiliferous grainstone with sporadic microfauna content (microfacies-4)	Ooids and peloids of two different sizes appear to be well-selected from the granulometric point of view.	Large mm-sized red algae, echinoids, and small forams	Dolomititic rock fragments with hydiotopic to hypidiotopic texture probably due to a contamination with another raw material	?
15	3714	USI-9	Fossiliferous wackestone with mm-sized benthic forams (microfacies-3)	Dark micritic matrix enriched with organic matter	Large benthic forams, i.e., Orbitolina, *Palorbitolinoides*, other pelagic forams, plus brachiopods, echinos, and gastropods	Organic carbon concentrated along stylolithes. Some veins are filled in by early diagenetic calcite cement.	Lower Cretaceous (Aptian)

Table 4. *Cont.*

(b)						
No.	**Code**	**Sample**	**Main components**	**Depositional texture**	**Diagenetic features**	**Cathodoluminescence (CLM)**
16	1882	QSC-2	Breccia-like texture composed of non-planar xenotopic to planar euhedral idiotopic mosaic of brownish zoned dolomite crystals (microfacies-5)	Probably ghostly peloidal texture with rare sub mm-sized plates of echinoids	Very fractured portions presenting large porosity filled in by zoned rhombohedral brownish mosaic of dolomite crystals. Subordinately, layered non-planar xenotopic mosaic. Organic carbon soaks fractures and interstitial matrix.	Mostly dull red luminescent matrix with bright red insoluble residue along seams and occasional bright spots of calcite. Dull red to non-luminescent, sometimes zoned, or brecciated, large saddle dolomite crystals, replacing brighter luminescent microcrystalline dolomite. Sporadic vuggy filling with thicker dull zoned and brighter rims. Last generation of cements with greenish rims maybe indicating high Sr content
17	2309	USI-10	Planar subhedral mosaic of brownish dolomite crystals with sporadic intercrystalline porosity (microfacies-7)	Not present	Packed mosaic of xenotopic dolomite crystals with lobate boundary shape alternates with mosaic of loosely packed idiotopic-hypidiotopic crystals with amoeboid boundary shape and high moldic intercrystalline porosity.	Non-luminescent saddle dolomite accompanied by bright luminescent insoluble residue. occasional bright luminescent overgrowths on larger dolomite crystals. Additionally, the vuggy filled dolomite cement appears dull luminescent, while the overgrowths exhibit bright luminescence.
18	3108	USI-11	Breccia-like texture composed of planar euhedral idiotopic mosaic of brownish zoned dolomite crystals, fractures, and isolated portions of parental rock, i.e., ghostly peloidal and fossiliferous limestone (microfacies-5)	Ghosts of peloidal and fossiliferous packstone with bivalvia and probably echinoid plates fragments	A breccia-like rock is dominant with non-planar hydiotopic zoned crystals of dolomite. Subordinated xenotopic-to-hypidiotopic mosaics are also present, characterized by dark fine-grained micritic inclusions. Sporadic chert replacements along secondary porosity.	Dull to bright red luminescent matrix, with possible calcite remains, microcrystalline dolomite, and two generations of pore-filling dolomite. Dull red luminescence and brighter rims indicating zoned saddle dolomite crystals.
19	3228	USI-12	Packed mosaic of hypidiotopic equigranular zoned dolomite crystals with lobate boundary shape (microfacies-8)	Ghosts of peloidal and fossiliferous packstone-to-grainstone	Porphyrotopic dolomite mosaic rock with sub-euhedral and zoned dolomite crystals dispersed in a fine-grained matrix. Equigranular fine-grained mosaic of subhedral dolomite crystals. Zoned subhedral inequigranular dolomite crystals with large secondary calcite cement fillings. Sporadic chert replacements along secondary porosity.	Interlocking dolomite mosaic characterized by crystals with cloudy centers and clear overgrowths. The centers of the crystals are non-luminescent, while the overgrowths display a bright red luminescence. The presence of patches of orange luminescence in the matrix suggests the possible presence of residual calcite. Additionally, smaller idiomorphic dolomite crystals are incorporated within larger saddle dolomite crystals. Some saddle dolomite crystals show signs of corrosion and/or micro brecciation.
20	3238	USI-13	Porous peloidal and fossiliferous dolomitic wackestone (microfacies-6)	Dark microcrystalline matrix is dominant. Presence of benthic forams, gastropods, and bivalve microfossils	This sample is a primary dolostone. No diagenetic dolomite replacements.	Dominant dull red luminescent matrix and dull to bright orange clasts

Table 4. *Cont.*

No.	Code	Sample	Main components	Depositional texture	Diagenetic features	Cathodoluminescence (CLM)
21	3239	USI-14	Porous peloidal and fossiliferous dolomitic wackestone (microfacies-6)	Dark microcrystalline matrix is dominant. Presence of benthic forams, gastropods, and bivalve microfossils	This sample is a primary dolostone. No diagenetic dolomite replacements.	Dominant dull red luminescent to bright orange biotic and abiotic clasts
22	3353	USI-15	Equigranular mosaic of brownish rhombohedral dolomite crystals, presenting ghost traces of the parental limestone texture (microfacies-8)	Ghosts of peloidal and fossiliferous packstone-to-grainstone. sporadic grains of a fossiliferous wackestone probably coming from the contamination from another raw material	Equigranular to non-equigranular mosaic of rhombohedral brownish crystals of dolomite. Irregular and diffused areas of very fine crystals in a coarse mosaic groundmass.	Bright red dolomite matrix with larger dolomite crystals exhibiting variations in luminescence and the presence of dark spots, possibly quartz or anhydrite grains. Sometimes brecciated fabric is observed, featuring a bright red luminescent matrix composed of microcrystalline dolomite and insoluble residue. The larger dolomite crystals and intraclasts show a range of luminescence, with brighter rims or overgrowths. Additionally, there is bright luminescent dolomite cement present in vugs and molds
23	3387	USI-16	Equigranular mosaic of fine-to-medium grained brownish dolomite crystals (microfacies-8)	Not present	Hydiotopic-to-hypidiotopic mosaic of dolomite crystals. Sporadic large porosity filled in by brownish and zoned saddle dolomite crystals.	Idiomorphic equigranular dolomite crystals. The crystals have cloudy centers and clear rims. Pore linings are characterized by bright red luminescent cements, primarily as overgrowths from the dolomite crystals. Additionally, there may be a presence of bright luminescent insoluble residue.

Table 5. Chemical analysis by WD-XRF on carbonate rock samples: limestones (no. 1–15) and dolostones (no. 16–23). Acronyms legend: LDL = lower detection limit (0.01 wt%); LOI = loss on ignition; IR = insoluble residue. The insoluble residue (IR) extracted by a pre-treatment procedure is also reported.

No.	Sample	LOI	SiO_2	Al_2O_3	Fe_2O_3	CaO	MgO	SO_3	Na_2O	K_2O	MnO	SrO	P_2O_5	TiO_2	Cl-	SUM	IR
		wt%	wt%	wt%	wt%	wt%	wt%	wt%	wt%	wt%	wt%	wt%	wt%	wt%	wt%	wt%	wt%
1	HOS-1	43.89	0.17	0.06	0.08	55.11	0.45	0.03	0.02	0.12	0.01	0.03	0.01	0.03	<0.01	100.0	0.40
2	HOS-2	41.97	1.78	0.28	0.28	50.97	2.17	0.74	0.16	0.09	0.01	1.44	0.02	0.02	0.08	100.0	3.02
3	HOS-3	43.82	0.28	0.10	0.14	55.11	0.34	0.04	0.01	0.12	0.01	0.03	<0.01	0.03	<0.01	100.0	0.46
4	HOS-4	43.22	1.19	0.34	0.33	52.11	2.55	0.07	0.01	0.01	0.01	0.08	0.01	0.07	0.01	100.1	2.49
5	HOS-5	43.48	1.33	0.39	0.21	52.43	1.72	0.10	0.07	0.16	0.01	0.06	0.01	0.03	<0.01	100.0	2.55
6	QSC-1	44.11	0.19	0.04	0.05	54.75	0.44	0.06	0.06	0.12	0.00	0.03	0.01	0.02	<0.01	99.9	0.34
7	USI-1	43.94	0.21	0.04	0.05	54.33	0.84	0.49	<0.01	0.03	0.01	0.03	0.03	<0.01	<0.01	100.0	0.61
8	USI-2	43.70	0.52	0.22	0.16	54.13	1.09	0.04	<0.01	0.08	0.00	0.03	0.01	0.03	<0.01	100.0	1.11

Table 5. *Cont.*

No.	Sample	LOI	SiO_2	Al_2O_3	Fe_2O_3	CaO	MgO	SO_3	Na_2O	K_2O	MnO	SrO	P_2O_5	TiO_2	Cl-	SUM	IR
9	USI-3	43.86	0.07	0.08	0.06	55.12	0.68	0.07	0.00	0.02	0.00	0.03	0.01	0.00	0.01	100.0	0.48
10	USI-4	43.03	0.45	0.08	0.03	55.76	0.49	0.06	0.01	0.03	0.01	0.03	0.02	0.01	0.01	100.0	2.44
11	USI-5	44.03	0.06	0.05	0.04	55.15	0.46	0.05	0.03	0.02	0.01	0.01	0.01	0.00	0.10	100.0	0.15
12	USI-6	43.98	0.35	0.11	0.11	54.62	0.64	0.07	0.01	0.04	0.01	0.03	0.02	0.01	0.01	100.0	0.72
13	USI-7	43.61	0.42	0.07	0.04	55.08	0.44	0.05	0.01	0.13	<0.01	0.02	0.03	0.01	<0.01	99.9	0.62
14	USI-8	44.10	0.24	0.13	0.11	51.86	3.40	0.04	<0.01	0.04	<0.01	0.03	0.04	<0.01	0.02	100.0	0.42
15	USI-9	43.69	0.18	0.07	0.05	55.41	0.48	0.04	0.01	0.03	<0.01	0.03	0.01	0.01	0.01	100.0	0.38
16	QSC-2	46.86	1.59	0.03	0.06	30.60	20.40	0.01	0.04	0.13	0.01	0.01	0.05	0.01	0.01	99.8	0.87
17	USI-10	47.64	0.20	0.07	0.12	30.58	21.05	0.19	<0.01	0.03	0.01	0.01	0.02	0.01	0.02	99.9	0.33
18	USI-11	46.70	0.29	0.01	0.03	32.59	20.24	0.03	0.02	0.03	0.01	0.02	0.03	<0.01	0.01	100.0	0.48
19	USI-12	47.72	0.27	0.06	0.11	31.23	20.25	0.11	0.12	0.02	0.01	0.01	0.01	0.01	0.08	100.0	0.45
20	USI-13	47.31	0.77	0.11	0.14	29.59	21.79	0.10	0.13	0.03	0.01	0.01	0.01	0.01	0.02	100.0	0.66
21	USI-14	47.75	0.65	0.10	0.09	29.51	21.58	0.09	0.09	0.02	0.01	0.08	<0.01	0.01	0.01	100.0	0.79
22	USI-15	45.95	0.58	0.12	0.08	36.96	15.79	0.40	0.08	0.01	<0.01	0.02	0.01	0.01	<0.01	100.0	0.88
23	USI-16	47.32	0.20	0.08	0.07	32.29	19.86	0.01	0.04	0.11	0.01	0.01	<0.01	<0.01	<0.01	100.0	0.36

Table 6. (**a**). Quantitative phase analysis by X-ray powder diffraction (XRPD-QPA) on whole carbonate rock samples: limestones (no. 1–15) and dolostones (no. 16–23). QPA values are recalculated from the weight fractions of insoluble residues and their XRPD-QPA analyses (refer to (**b**)). (**b**). Quantitative phase analysis by X-rays powder diffraction (XRPD-QPA) on insoluble residues. Legend of mineral phases and symbols: Cal = calcite; Dol = dolomite; Qtz = quartz; Mic = micaceous mineral (illite/muscovite); Sme = smectites; Kln = kaolinite, Chl = chlorite; Ant = antigorite; Plg = palygorskite; Kfs = K-feldspar; Pl = Plagioclase; Ep = epidote; Amp = amphibole; Gt = goethite; Hem = hematite; Py = pyrite; Gp = gypsum; Cel = Celestine; Rt = rutile; Fl = fluorite: Tr = traces (<0.1 wt%).

(a)

No.	Sample	Cal	Dol	Qtz	Mic	Sme	Kln	Chl	Ant	Plg	Kfs	Pl	Ep	Amp	Gt	Hem	Py	Gp	Cel	Rt	Fl
		wt%	wt%	wt%	wt%	wt%	wt%	wt%	wt%	wt%	wt%	wt%	wt%	wt%	wt%	wt%	wt%	wt%	wt%	wt%	wt%
1	HOS-1	99.6		Tr	0.2	Tr	Tr				Tr				0.1	Tr					
2	HOS-2	86.4	10.4	0.6	0.9					0.1	Tr	Tr			0.2			0.2	1.1		

Table 6. *Cont.*

(a)

No.	Sample	Cal	Dol	Qtz	Mic	Sme	Kln	Chl	Ant	Plg	Kfs	Pl	Ep	Amp	Gt	Hem	Py	Gp	Cel	Rt	Fl
		wt%	wt%	wt%	wt%	wt%	wt%	wt%	wt%	wt%	wt%	wt%	wt%	wt%	wt%	wt%	wt%	wt%	wt%	wt%	wt%
3	HOS-3	99.5	Tr	Tr	0.2	Tr	Tr	Tr			Tr	Tr			0.1	0.1				Tr	
4	HOS-4	85.4	12.1	0.5	0.8	0.4	Tr	0.2	0.1	0.3		0.1			0.1						
5	HOS-5	90.0	7.5	0.4	0.9		Tr	0.1		Tr	0.8	Tr			Tr	0.1			0.2	Tr	
6	QSC-1	99.7		0.2	0.1	Tr			Tr	Tr	Tr				Tr		Tr				
7	USI-1	96.4	3.0	0.1	0.3	0.1		Tr		Tr	0.1				Tr						
8	USI-2	98.9		0.1	0.8						0.1				0.1						
9	USI-3	99.5		0.2	0.2		Tr	Tr							0.1						
10	USI-4	97.6		0.5	0.2																1.7
11	USI-5	99.8		Tr	0.1	Tr	Tr	Tr			Tr				Tr	Tr					Tr
12	USI-6	99.3		0.2	0.5				Tr		Tr				Tr	Tr					
13	USI-7	99.4		0.3	0.2	Tr		Tr						Tr	Tr						
14	USI-8	84.0	15.6	0.1	0.1		0.1	Tr							0.1						
15	USI-9	99.4	0.2	0.2	0.2	Tr							Tr		Tr						
16	QSC-2	3.4	95.7	0.8	Tr	Tr															
17	USI-10	3.7	96.1	Tr	0.1	Tr	Tr					Tr			Tr	Tr					
18	USI-11	6.9	92.6	0.5																	
19	USI-12	6.3	93.3	0.2	0.1	0.1	Tr					Tr			Tr		Tr				
20	USI-13		99.3	0.2	0.3					0.2	Tr				Tr		Tr				
21	USI-14		99.2	0.2	0.1					0.2	0.1				0.1		Tr				
22	USI-15	27.2	72.0	0.4	0.1	Tr	Tr			Tr	0.3				Tr		Tr				
23	USI-16	9.3	90.4	0.1	0.2	Tr	Tr	Tr		Tr		Tr			Tr		Tr				

(b)

No.	Sample	IR	Qtz	Mic	Sme	Kln	Chl	Ant	Plg	Kfs	Pl	Ep	Amp	Gt	Hem	Py	Cel	Rt	Fl
		wt%	wt%	wt%	wt%	wt%	wt%	wt%	wt%	wt%	wt%	wt%	wt%	wt%	wt%	wt%	wt%	wt%	wt%
1	HOS-1	0.40	0.8	56.0	7.0	6.7				2.4				21.7	4.4			1.0	
2	HOS-2	3.02	19.4	31.5					3.0	1.4	0.5			7.1			37.2		
3	HOS-3	0.46	1.6	36.0	1.5	5.9	4.4			10.7	1.0			12.7	20.2			6.0	

Table 6. *Cont.*

No.	Sample	IR	Qtz	Mic	Sme	Kln	Chl	Ant	Plg	Kfs	Pl	Ep	Amp	Gt	Hem	Py	Cel	Rt	Fl
		wt%	wt%	wt%	wt%	wt%	wt%	wt%	wt%	wt%	wt%	wt%	wt%	wt%	wt%	wt%	wt%	wt%	wt%
4	HOS-4	2.49	20.1	32.3	16.9	1.4	6.4	2.2	13.7		4.6			2.5					
5	HOS-5	2.55	15.9	36.9		1.4	4.2		1.7	29.8				0.4	2.0		6.0	1.7	
6	QSC-1	0.34	45.4	42.0	2.6			0.2	1.9	4.2				0.6		3.2			
7	USI-1	0.61	10.7	45.2	17.3		1.7		4.0	13.3				7.8					
8	USI-2	1.11	11.6	72.5						5.1				10.8					
9	USI-3	0.48	38.6	43.2		6.4	0.4							11.4					
10	USI-4	2.44	21.6	7.5															70.9
11	USI-5	0.15	8.6	38.4	1.0	3.7	1.2			25.6				15.7	1.0				4.7
12	USI-6	0.72	24.7	66.7				0.7		0.7				6.3	0.9				
13	USI-7	0.62	50.5	35.5	4.6	1.3							1.8	6.4					
14	USI-8	0.42	23.2	18.4		27.8	3.6							27.0					
15	USI-9	0.38	40.0	46.5	10.0							1.5		2.0					
16	QSC-2	0.87	95.2	3.9	0.9														
17	USI-10	0.33	18.5	32.0	12.9		4.7				11.0			20.2	0.7				
18	USI-11	0.48	100.0																
19	USI-12	0.45	42.2	27.3	11.7	8.6					0.6			8.7		0.9			
20	USI-13	0.66	25.8	38.9					28.4	4.5				1.6		0.9			
21	USI-14	0.79	30.9	14.1	1.0				28.9	6.7				17.0		1.5			
22	USI-15	0.88	45.7	11.1	0.2	0.7			4.2	33.8				2.4		1.8			
23	USI-16	0.36	20.0	52.7	2.0	8.2	0.5		6.3		2.6			5.6		2.0			

Microfacies no. 1: white, light gray, yellow, reddish-yellow, and very pale brown, fairly porous, medium- to coarse-grained fossiliferous limestones from different Iranian deposits (HOS-1, HOS-2, HOS-3, HOS-4), plus one sample (USI-1) of undermined provenance (see Table 1 and Figure 2A). Limestones in this group consist mainly of grain-supported microfacies, i.e., poorly sorted fossiliferous packstone, laterally transitioning to mud-supported microfacies, i.e., fossiliferous peloidal wackestone (Table 4, part a). Typical micro-fossiliferous association is represented by large mm-sized benthic forams, including *Nummulites*, *Orbitolites*, and *Milioids*, plus bivalves, bryozoans, brachiopods, echinoderms, and crinoids of Paleogene to Neogene (i.e., Ypresian to Priabonian for samples HOS-1, HOS-2, HOS-3, USI-1, and Oligocene-Miocene for sample HOS-4, see Table 4, part a). Bioclastic fragments are embedded in a residual dark micritic matrix under XPL, enriched in organic carbon, clay minerals, and other subordinate siliciclastic grains. The insoluble residue, between 0.4 and 3.2 wt%, is mainly composed of micaceous minerals (0.2–0.8 wt%), quartz (0.05–0.6 wt%), K-feldspar (traces), iron oxides and hydroxides (traces), sporadic plagioclase (max 0.3 wt%), palygorskite (max 0.3 wt%), rutile (traces), and minor other clay minerals, including smectite, kaolinite, and clinochlore (see Table 6, part a). Exceptionally, sample HOS-2 is characterized by the presence of celestine (1.1 wt%) and gypsum (0.2 wt%). The mold porosity is mostly filled by microsparite and/or mosaic cement. Neomorphic cement also fills some secondary veins. Samples HOS-2, HOS-4, and USI-1 also show penecontemporaneous dolomitization.

Microfacies no. 2: pale yellow to very pale brown, fairly porous, medium-grained fossiliferous limestones coming from Iranian deposits (HOS-5 and USI-5; see Table 1 and Figure 2A,B). Limestones of this group are composed of mud-supported microfacies, i.e., fossiliferous peloidal wackestone, transitioning to grain-supported microfacies, i.e., poorly sorted fossiliferous packstone (see Table 4, part a). The typical micro-fossiliferous association is composed of benthic forams (i.e., *Nezzazzata* sp.?, *Edomia reicheli*, *Multispira* sp.?, *Trocholina* sp., *Miliolids*), plus gastropods, bivalves, red algae, and bryozoan fragments belonging to the Lower-Upper Cretaceous (Late Cenomanian for sample HOS-5, Early Middle Cretaceous for sample USI-5). Bioclasts and fossils are embedded in an abundant dark micritic matrix under XPL, enriched in organic carbon. The insoluble residue, ranging from 0.2 to 2.6 wt%, is composed of micaceous minerals (0.1–0.9 wt%), quartz (max 0.9 wt%), K-feldspar (max 0.8 wt%), celestine (0.2 wt%), iron oxides and hydroxides (traces), rutile (traces), fluorite (traces), and, to a lesser extent, other clay minerals (Table 6, part a). Vuggy voids and mold porosity in these samples are largely filled by early diagenetic cement. The sample HOS-5 also shows penecontemporaneous dolomitization.

Microfacies no. 3: dark and very dark gray to grayish brown, sporadically very light brown, fine-grained fossiliferous limestones declared or suspected to be from the Stevin Rock deposit in the UAE (QSC-1, USI-2, USI-4, and USI-9, see Table 1 and Figure 2A,B). Limestones of this group are mainly composed of mud-supported microfacies, i.e., fossiliferous wackestone, characterized by large mm-sized benthic forams with dominant *Orbitolinids* (i.e., *Palorbitolina* sp., *Salpingoporella dinarica*, *Palorbitolinoides* sp., see Table 4, part a), sporadic *Ostrea* fragments, large plates of echinoids, gastropods, crinoids, and peloidal coated grains embedded in a dark brown micritic matrix under XPL. The micro-fossiliferous assemblage is typical of the Lower Cretaceous (Upper Barremian to Lower Aptian). The insoluble residue, which ranges between 0.3 and 2.4 wt%, is mainly composed of micaceous minerals (0.1–0.8 wt%), quartz (0.1–0.5 wt%), goethite (traces), feldspars (traces), epidote (traces), pyrite (traces), and, to a lesser extent, other clay minerals, including smectite and palygorskite (see Table 6, part a). Exceptionally, the sample USI-4 is also characterized by the presence of fluorite (1.7 wt%).

Microfacies no. 4: light gray to gray, medium to coarse-grained limestone from the Gulf Rock (USI-3, USI-6, and USI-7) and Jawhart (USI-8) deposits in the UAE (Table 1 and Figure 2A,B). The limestones of this group are mainly composed of grain-supported microfacies, i.e., ooidal-peloidal and fossiliferous grainstone. Ooidal and peloidal grains are dimensionally well-selected with a grain size between 200 and 400 μm. They are composed

at the core of a coated grain or a bioclast, such as sporadic detrital quartz, or tiny forams, echinoid spines, and plates. Several large sub-millimeter-sized lumped aggregates are also present Figure 4. Intraclastic porosity is filled by early diagenetic microsparite and/or mosaic cement. Large plates of echinoids often have a characteristic epitaxial cement rim. Secondary veins are filled by neomorphic mosaic cement. The micro-fossiliferous assemblage is typical of the Lower-Upper Cretaceous period (likely Cenomanian for sample USI-3, Berriasian-Valanginian for sample USI-6; see Table 4, part a). The insoluble residue, which ranges between 0.4 and 0.7 wt%, is mainly composed of micaceous minerals (0.1–0.5 wt%), quartz (0.1–0.3 wt%), goethite (traces), plus subordinately, other clay minerals (Table 6, part a). Sample USI-8 also shows some penecontemporaneous dolomitization.

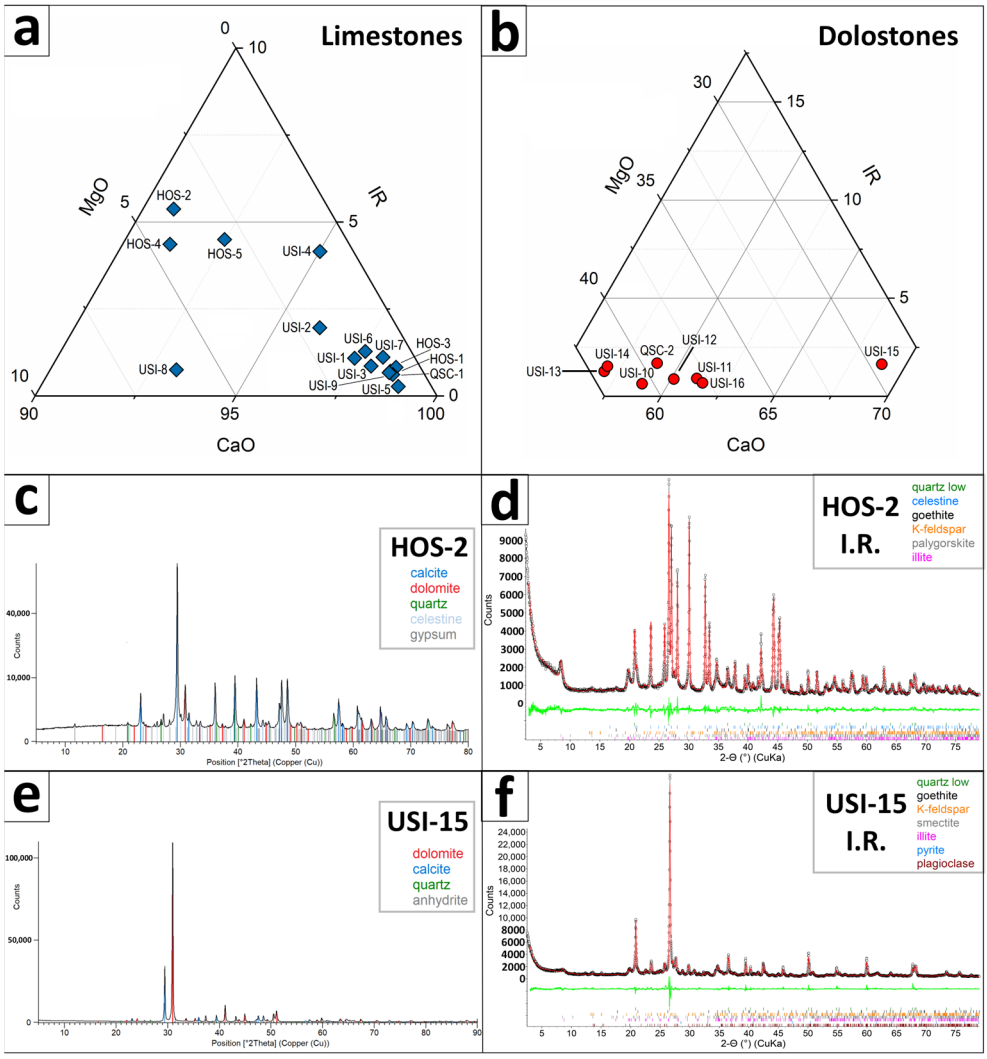


Figure 4. Chemical triangular diagrams and X-ray Powder Diffraction (XRPD) analyses of two representative carbonate rock samples: (**a**) triangular diagram (CaO-MgO-IR) of limestone samples; (**b**) triangular diagram (CaO-MgO-IR) of dolostone samples; (**c**) XRPD analysis of limestone sample HOS-2; (**d**) Rietveld refinement plot of the insoluble reside of sample HOS-2; (**e**) XRPD analysis of dolostone sample USI-15; (**f**) Rietveld refinement plot of the insoluble reside of sample USI-15.

Microfacies no. 5: light gray to gray mostly cataclastic dolostone reported or suspected to originate from Stevin Rock, UAE (USI-11 and QSC-2; see Table 1 and Figure 2C). Dolostones belonging to this group typically have a medium- to coarse-grained breccia-like texture, mostly composed of a planar euhedral idiotopic mosaic of brownish-zoned saddle dolomite crystals. Fractures are generally saturated with organic carbon and interstitial matrix. Some parts of the rock show ghostly remnants of fossiliferous-peloidal packstone

(Table 4, part b). Saddle dolomite and matrix are dull red. Solution seems and rim overgrowths of saddle dolomite are bright red under CLM (see Figure 3). They represent the late stage of diagenetic cementation. The insoluble residue, ranging between 0.5 and 0.9 wt%, is mostly quartz with traces of clay minerals (i.e., a micaceous mineral and some smectite, Table 6, part a).

Microfacies no. 6: pale yellow to white, extremely porous dolostones of undermined provenance (USI-13 and USI-14, see Table 1, Figures 2C and 3). Samples have a mud-supported primary texture, meaning that they are probably precipitated in situ. The typical feature is a dolomitic wackestone with significant fossiliferous content, including benthic forams, gastropods, and bivalves. Matrix is mostly dull red under CLM, while the biotic and abiotic clasts are bright orange (see Figure 3). The insoluble residue, which ranges between 0.7 and 0.8 wt%, consists mainly of quartz, feldspars (i.e., plagioclase and K-feldspar), a micaceous mineral, goethite, and traces of pyrite and smectite (Table 6, part b).

Microfacies no. 7: light gray to yellowish brown and brownish gray fine-grained dolostone of undermined provenance (USI-10) (see Table 1 and Figure 2C). Typical texture consists of a non-planar xenotopic to planar-subhedral hypidiotopic mosaic of mostly brownish lobate-zoned dolomite crystals. Subordinated planar-euhedral idiotopic mosaic is sometimes present. Sporadic to frequent intercrystalline porosity is filled by microsparite cement. Rare microcrystalline quartz replacements (Table 4, part b). Saddle dolomite is mostly non-luminescent. Conversely, dolomite crystal overgrowths are brightly luminescent, as is the insoluble residue. In addition, vuggy fillings appear dull luminescent. The insoluble residue is 0.3 wt% and consists mainly of a micaceous mineral, goethite, quartz, plagioclase, smectite, and traces of clinochlore (Table 6, part a).

Microfacies no. 8: very pale brown, quite porous, medium- to coarse-grained dolomite rock from Bushehr, Iran (USI-12). A couple of samples whose provenance is not given (USI-15 and USI-16; see Table 1 and Figure 2C) also belong to this microfacies. Typical microstructure shows a planar-euhedral idiotopic to planar-subhedral hypidiotopic mosaic of zoned dolomite crystals (Table 4, part b). Sporadic large porosity is filled by brownish zoned saddle dolomite. Under CLM, idiomorphic equigranular dolomite crystals show variations in luminescence. Sometimes a brecciated fabric is observed with a bright red luminescent matrix of microcrystalline dolomite and insoluble residue. The larger dolomite crystal overgrowths, intraclasts, and dolomitic cement in vugs and molds show a brighter red luminescence (see Figure 3). The insoluble residue, ranging from 0.4 up to 0.9 wt%, consists mainly of quartz, a micaceous mineral, feldspars (i.e., plagioclase and K-feldspar), goethite, and traces of smectite, kaolinite, and pyrite (Table 6, part a).

4.2. Isotopic Signature and Source Deposits

C-O isotopic analysis ($\delta\ ^{13}C$ and $\delta\ ^{18}O$) was carried out on a total of 28 samples. Of these, 23 samples were "bulk" limestones and dolostones, while the remaining 5 samples were obtained by dissolution of calcite (HOS-2, HOS-3, HOS-5, USI-8, and USI-15, as shown in Table 5). Results are reported in Table 7; moreover, Figure 5a,b shows the results categorized by source deposits and carbonate rock microfacies, respectively.

Table 7. C-O stable and Sr isotopic analyses of samples from the Arabian Peninsula and neighboring countries. Symbols legend: Acd = After calcite dissolution; VPDB = Vienna Pee Dee Belemnite standard; Nd = not determined.

No.	Sample	Type	Bulk/Acd	Declared Provenance	Real Provenance	$\delta^{18}O$ (VPDB)	$\delta^{13}C$ (VPDB)	Std Corrected. $^{87}Sr/^{86}Sr$
1	HOS-1	Lmt	bulk	Mirzaei, Iran	Iran	−6.14	1.48	0.707894
2-a	HOS-2a	Lmt	bulk	Baqiabad, Iran	Baqiabad, Iran	−2.83	0.46	0.707953
2-b	HOS-2b	Dol	Acd	Baqiabad, Iran	Baqiabad, Iran	−2.64	0.61	Nd
3	HOS-3	Lmt	bulk	Angoran, Iran	Angoran, Iran	−6.28	1.72	0.707902
4-a	HOS-4a	Lmt	bulk	Kashigari, Iran	Iran	−2.89	0.63	0.708854
4-b	HOS-4b	Dol	Acd	Kashigari, Iran	Iran	−2.64	0.55	Nd
5-a	HOS-5a	Lmt	bulk	Dargaz, Iran	Dargaz, Iran	−5.13	0.49	0.708816
5-b	HOS-5b	Dol	Acd	Dargaz, Iran	Dargaz, Iran	−5.63	0.48	Nd
6	QSC-1	Lmt	bulk	Nd	Stevin Rock, UAE	−4.33	2.80	0.708174
7	USI-1	Lmt	bulk	Nd	Unknown site no. 1	−5.52	−3.45	0.707834
8	USI-2	Lmt	bulk	Stevin Rock, UAE	Stevin Rock, UAE	−3.90	2.72	0.708252
9	USI-3	Lmt	bulk	Gulf Rock, UAE	Gulf Rock, UAE	−2.73	1.39	0.707616
10	USI-4	Lmt	bulk	Stevin Rock, UAE	Stevin Rock, UAE	−6.01	3.72	0.707862
11	USI-5	Lmt	bulk	Iran	Dargaz, Iran	−4.71	−0.22	0.707490
12	USI-6	Lmt	bulk	Nd	Gulf Rock, UAE	−3.09	1.49	0.707704
13	USI-7	Lmt	bulk	Nd	Gulf Rock, UAE	−2.83	1.72	0.707712
14-a	USI-8a	Lmt	bulk	Jawhart, UAE	Jawhart, UAE	−3.06	−0.27	0.707692
14-b	USI-8b	Dol	Acd	Jawhart, UAE	Jawhart, UAE	−3.09	−0.71	0.707560
15	USI-9	Lmt	bulk	Stevin Rock, UAE	Stevin Rock, UAE	−3.53	2.97	0.708304
16	QSC-2	Dol	bulk	Nd	Stevin Rock, UAE	−2.47	3.48	0.708855
17	USI-10	Dol	bulk	Nd	Unknown site no. 2	−8.73	3.87	0.707634
18	USI-11	Dol	bulk	Stevin Rock, UAE	Stevin Rock, UAE	−4.23	2.34	Nd
19	USI-12	Dol	bulk	Bushehr, Iran	Bushehr, Iran	−2.47	−1.76	0.707791
20	USI-13	Dol	bulk	Nd	Unknown site no. 3	−0.67	−0.59	0.707774
21	USI-14	Dol	bulk	Nd	Unknown site no. 3	−0.41	−0.61	0.707757
22-a	USI-15a	Dol	bulk	Nd	Jawhart, UAE	−3.19	−1.58	0.707893
22-b	USI-15b	Dol	Acd	Nd	Bushehr, Iran	−1.95	−0.63	0.707702
23	USI-16	Dol	bulk	Nd	Bushehr, Iran	−2.89	−3.10	0.707536

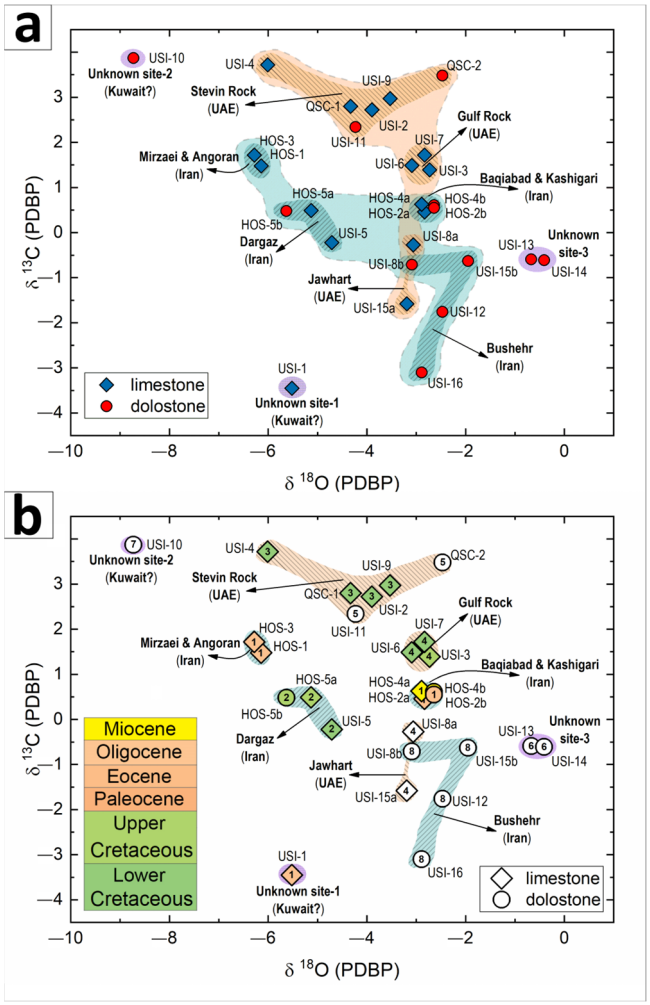


Figure 5. C–O stable isotopes distribution of limestone and dolostones. $\Delta^{13}C$ and $\delta^{18}O$ data are expressed relative to the PDB standard according to Craig [51]. The investigated samples are grouped by source deposits in (**a**), and by microfacies (no. 1–8, see Section 4.1) and ages in (**b**), respectively.

The isotopic values for all the samples analyzed range between 3.87 and −3.45‰ for $\delta^{13}C$ with an average of 0.71 (standard deviation = 1.9). For $\delta^{18}O$, the values range from −0.41 to −8.73 with an average of −3.71 (standard deviation = 1.8). The isotopic C/O cross plots show distinct subpopulations of data corresponding to the provenance and microfacies. Furthermore, a significant difference in isotopic values between calcite and dolomite, except for dolomitic samples obtained after the calcite dissolution (HOS-2, HOS-4, and HOS-5), which closely resemble the isotopic composition of the corresponding bulk rock samples, is observed. However, this similarity does not hold for two samples (USI-8 and USI-15), indicating that they are probably derived from a mixture of two different raw materials. Plant results have corroborated this fact, demonstrating alternating quicklime and dololime production campaigns (refer to Supplementary Materials Table S3 for further details). Specifically, the calcitic component of these samples appears to be derived from microfacies 3 (peloidal-fossiliferous limestone, as described in Table 4, part a) from Jawhart, UAE. In contrast, the dolomitic portion of the same samples is composed of microfacies 8 (hypidiotopic mosaic of dolomite crystals, as described in Table 4, part b) from Bushehr, Iran. The subpopulations of the source deposits can be distinguished based on Figure 5 as follows:

- Stevin Rock, UAE (USI-2, USI-4, USI-9, USI-11, QSC-1, and QSC-2);
- Gulf Rock, UAE (USI-3, USI-6, and USI-7);
- Mirzaei-Angoran, Iran (HOS-1 and HOS-3);

- Dargaz, Iran (HOS-5 and USI-5);
- Baqiabad-Kashigari, Iran (HOS-2 and HOS-4);
- Jawhart, UAE (USI-8a and USI-15a),
- Bushehr, Iran (USI-8b, USI-12, and USI-15b).

In addition, three unknown source sites have been identified:

- Site 1 (USI-1, likely from Kuwait);
- Site 2 (USI-10, likely from Kuwait);
- Site 3 (USI-13 and USI-14).

It is worth noting that the identified deposits predominantly exhibit homogeneous microfacies, features, and ages as classified in Section 4.1. This observation is depicted in Figure 5.

Currently, there are very few references for a Sr isotope database to trace the provenance of carbonate raw materials used in lime production. Therefore, the Sr isotope plot shown in Figure 6 serves as a starting point for future investigations. The samples have been grouped based on the source deposits identified by the combined analysis of the C-O isotopic signature and microfacies analysis. The Sr isotopic composition ranges from 0.708855 to 0.707490, with an average value of 0.707940. The highest value is reported for sample QSC-2, while the lowest value is observed in sample USI-5.

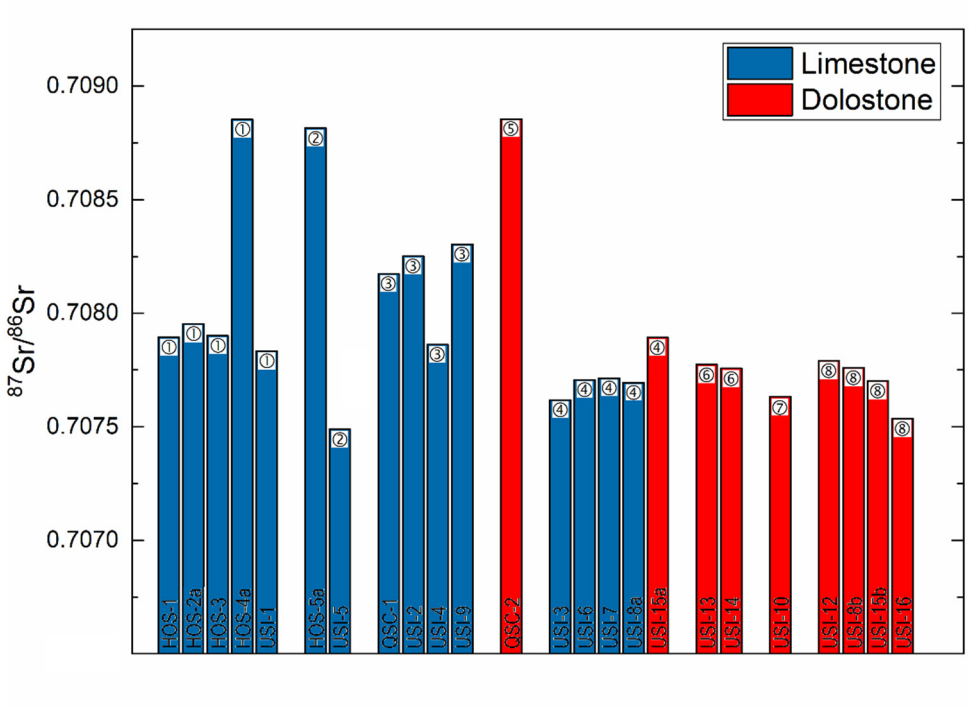


Figure 6. $^{87}Sr/^{86}Sr$ ratios of limestone and dolostones. Samples are grouped per type, provenance, and microfacies, respectively.

4.3. Slaking Reactivity

The results of the reactivity tests are given in Table 8 and plotted in Figure 7.

Table 8. Technological tests on quicklime and dololime samples burnt at 1050 °C and 1150 °C. Symbols legend: ΔT 40 °C (or t_{60}) for quicklimes, and ΔT 30 °C (or t_{50}) for dololimes, respectively; TAST = Total Active Slaking Time.

No.	Sample	Type	t_{60}/t_{50} 1050 °C	T_{max} 1050 °C	TAST 1050 °C	t_{60}/t_{50} 1150 °C	T_{max} 1150 °C	TAST 1150 °C	MD 10 mm	MD 19 mm	Drop Test	OBT Blocks Weight	Sticking Tendency
			min	°C	min	min	°C	min	wt%	wt%	wt%	g	wt%
1	HOS-1	Lmt	0.8	81.8	3.0	2.8	72.5	7.0	7.0	8.1	40.0	17.8	42.4
2	HOS-2	Lmt	4.9	67.4	8.5	15.8	61.5	14.5	18.2	19.7	51.3	11.5	27.4
3	HOS-3	Lmt	0.5	81.4	2.5	1.9	75.8	6.0	8.8	10.8	38.4	16.7	39.8
4	HOS-4	Lmt	2.1	74.5	5.5	6.2	68.9	10.5	34.9	38.9	60.2	11.8	28.1
5	HOS-5	Lmt	2.8	73.7	7.0	10.0	68.8	14.0	20.1	20.1	17.8	12.9	30.7
6	QCS-1	Lmt	0.6	78.3	3.0	2.9	71.6	6.5	11.2	17.3	29.9	17.0	40.5
7	USI-1	Lmt	0.9	80.7	4.0	1.3	72.0	4.0	17.9	37.1	60.1	16.1	38.2
8	USI-2	Lmt	0.4	80.3	2.5	2.7	72.4	7.0	8.1	17.3	27.7	13.5	32.2
9	USI-3	Lmt	0.8	75.6	3.5	1.9	75.5	6.5	11.6	34.6	22.6	11.1	26.4
10	USI-4	Lmt	0.7	76.1	3.0	1.9	75.1	5.0	26.7	21.5	36.7	10.3	24.5
11	USI-5	Lmt	0.3	83.2	2.5	Nd	Nd	Nd	10.7	22.3	23.8	18.0	42.8
12	USI-6	Lmt	1.4	74.6	5.0	2.5	73.6	6.0	23.0	32.3	44.9	19.2	45.7
13	USI-7	Lmt	0.4	80.1	2.0	0.8	80.4	3.5	19.2	23.4	27.8	17.5	41.7
14	USI-8	Lmt	0.3	79.7	2.5	Nd	Nd	Nd	15.3	32.0	26.6	16.7	39.7
15	USI-9	Lmt	0.7	78.6	4.0	0.9	78.5	4.5	8.5	15.4	29.4	14.4	34.3
16	QSC-2	Dol	0.4	57.9	1.5	0.4	56.8	1.5	10.9	23.5	36.1	6.0	15.3
17	USI-10	Dol	0.4	62.2	1.5	0.4	57.5	3.0	17.7	57.2	56.1	9.9	25.2
18	USI-11	Dol	0.4	58.5	1.5	0.4	70.0	1.5	25.2	37.3	49.7	2.8	7.0
19	USI-12	Dol	8.8	54.2	9.0	12.7	53.5	1.5	27.6	27.6	77.4	13.0	33.2
20	USI-13	Dol	3.0	53.3	4.5	3.3	54.7	5.5	67.0	77.4	39.0	14.2	36.3
21	USI-14	Dol	3.9	51.9	4.5	24.2	51.7	16.0	57.9	59.1	24.4	13.6	34.6
22	USI-15	Dol	0.7	65.6	3.0	11.0	53.0	10.5	38.7	41.2	59.7	10.4	26.5
23	USI-16	Dol	3.6	54.1	5.5	5.0	54.7	7.0	28.4	31.6	47.5	12.4	31.7

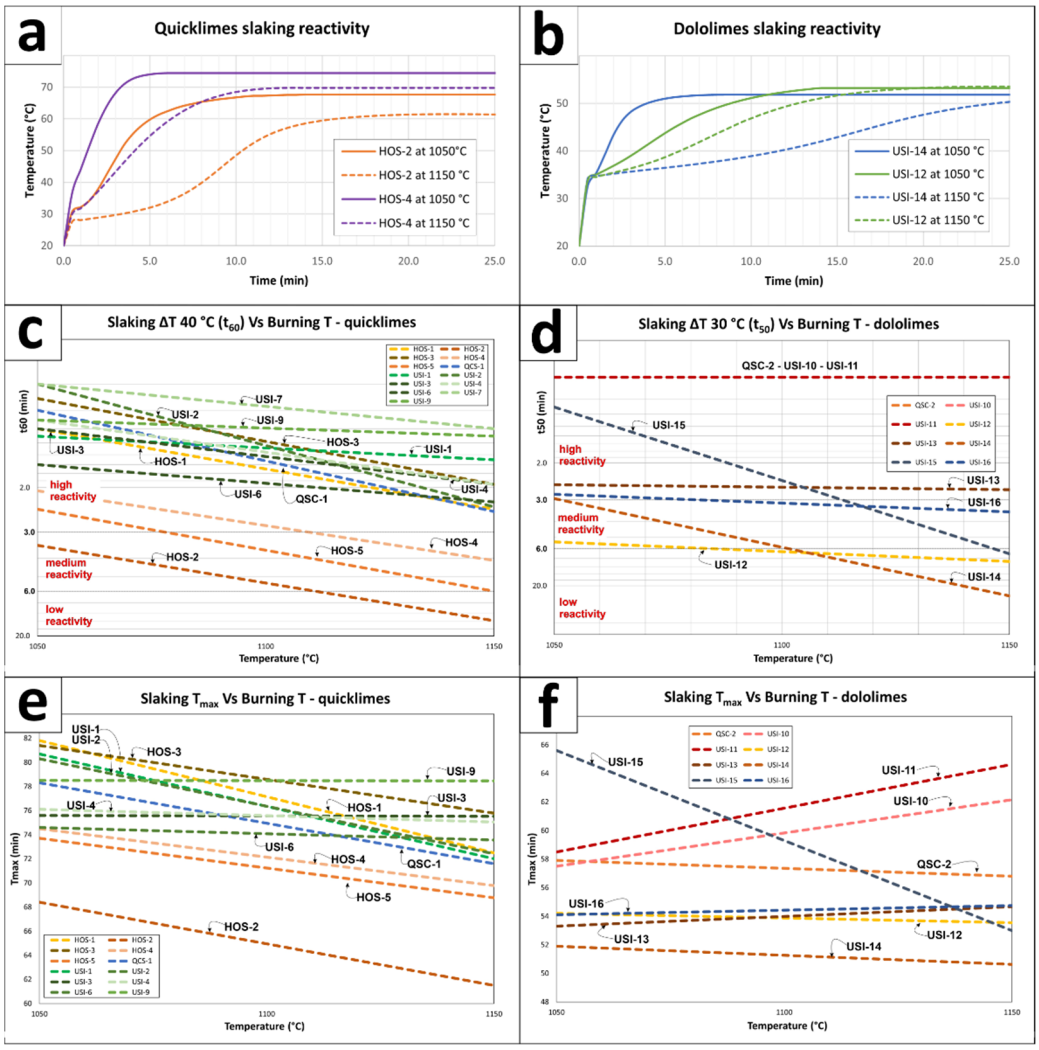


Figure 7. Reactivity plots of limes burnt at different temperature (i.e., 1050–1150 °C): (**a**,**b**) slaking curves of two representative quicklime and dololime samples; (**c**) slaking temperature rise, i.e., ΔT40 °C or t_{60} (min) against quicklime burning temperature (°C); (**d**) slaking temperature rise, i.e., ΔT30 °C or t_{50} (min) against dololime burning temperature (°C); (**e**,**f**) maximum slaking temperature, i.e., T_{max} (°C) against quicklime and dololime burning temperature (°C).

The quicklime burned at 1050 °C shows a temperature rise of 40 °C (referred to as t_{60}). This temperature rise occurs within a time range of 0.3 to 4.9 min, with an average time of 1.2 min. Furthermore, the maximum slaking temperature (referred to as T_{max}) of the quicklimes varies between 67.4 and 83.2 °C, with an average temperature of 77.7 °C. On the other hand, the dololimes burned at 1050 °C show a temperature increase of 30 °C (referred to as t_{50}). This temperature rise occurs within a time range of 0.4 to 8.8 min, with an average time of 2.7 min. In addition, the maximum slaking temperature (referred to as T_{max}) of the dololimes ranges between 51.9 and 65.6 °C, with an average temperature of 57.2 °C. For quicklime burned at 1150 °C, the t_{60} rise ranges from 0.5 to 15.8 min, with an average time of 4.0 min. The corresponding T_{max} is between 61.5 and 80.4 °C, with an average temperature of 72.8 °C. Finally, the t_{50} rise of dololimes burned at 1150 °C ranges between 0.4 and 24.2 min, with an average time of 7.2 min. The T_{max} for this case is between 51.7 and 70.0 °C, with an average temperature of 56.5 °C.

By subjecting raw materials of similar size fractions to comparable calcination conditions in a muffle furnace, including time, heating rate, and maximum burning temperatures, the variations in reactivity can be primarily attributed to the characteristics of the parent rocks and their impurity content, particularly the insoluble residue [8–10,52]. As a result,

the combination of mineralogical and petrographic features with the slaking reactivity at 1050–1150 °C has allowed the identification of two distinct groups of rocks with different tendencies to sinter or overburn [10]. These groups are described as follows (refer to Table 9).

The first group is represented by samples with very high reactivity (t_{60} < 1 min) at 1050 °C, and high reactivity (t_{60} = 2–3 min) at 1150 °C. In fact, these samples have a low tendency to overburn, as evidenced by the gentle slope of the t_{60}-t_{50} slaking curves plotted in Figure 7b. These samples can be classified according to their textures as grain-supported limestones (microfacies-1: samples HOS-1, HOS-3, USI-1, and USI-3), mud-supported limestones (microfacies-2: samples QSC-1, and USI-9), breccia-like dolostones (microfacies-4: samples QSC-2, and USI-11), and xenotopic mosaic dolostones (microfacies-5, sample USI-10). They always have a low impurity content (IR < 1.0 wt%).

The second group is represented by samples with high (t_{60} = 1–2 min) to medium-high (t_{60} = 2–4 min) reactivity at 1050 °C and low (t_{60} > 6 min) or very low reactivity (t_{60} > 10 min) at 1150 °C. In fact, these samples have a high tendency to overburn, as evidenced by the steep slope of the t_{60}-t_{50} slaking curves plotted in Figure 7b. These samples can be classified according to their textures as grain-supported limestones (microfacies-1: samples HOS-2, and HOS-4), mud-supported limestones (microfacies-2: samples HOS-5, USI-2, and USI-4), hypidiotopic dolostone (microfacies-8, sample USI-15), and mud-supported dolostones (microfacies-6: sample USI-14). They have a high impurity content (IR > 1.0 wt%).

Table 9. Different parameters affecting the sintering or overburning tendency of lime samples from the Arabian Peninsula and neighboring countries: rock fabric, including lithofacies and microfacies, impurity content, and reactivity at different burning temperatures.

Group	Lithofacies	Microfacies	Impurity Content	Reactivity at 1050 °C	Reactivity at 1150 °C	Overburning Tendency	Sample
1	Grain-supported, hypidiotopic and breccia-like texture	Microfacies-1 Microfacies-2 Microfacies-4 Microfacies-5	Low IR < 1.0 wt%	very high (t_{60} < 1 min) to high (t_{60} = 1–3 min)	high (t_{60} = 1–3 min) to medium-high (t_{60} = 3–4 min)	low gentle slope Figure 8	HOS-1 HOS-3 USI-1 USI-3 USI-6 USI-7 QSC-2 USI-11
	Mud-supported; and xenotopic texture	Microfacies-3 Microfacies-7					QSC-1 (USI-2) USI-9 USI-10
2	Grain-supported, and hypidiotopic	Microfacies-1 Microfacies-8	High IR > 1.0 wt%	high (t_{60} = 1–3 min) to medium-high (t_{60} = 3–4 min)	low (t_{60} > 6 min) to very low (t_{60} > 10 min)	high deep slope Figure 8	HOS-2 HOS-4 (USI-15)
	Mud-supported	Microfacies-2 Microfacies-3 Microfacies-6					HOS-5 (USI-2) USI-14

Lime samples from the first group are suitable for use in TSR kilns because their overall high reactivity is coupled with a low sintering tendency. Conversely, lime samples belonging to the second group can be considered critical for achieving the target reactivity required by steel producers (t_{60} or t_{50} < 1 min), especially when solid fuels are used in TSR kilns. It is therefore advisable to avoid samples HOS-2, HOS-4, HOS-5, USI-12, and USI-14 due to their consistently poor reactivity performance. However, sample USI-15 and, to a lesser extent, sample USI-4, which show a high reactivity at 1050 °C and a strong tendency to sinter, can be used specifically when the fuel type is natural gas. Finally, samples USI-12, USI-13, and USI-16, which do not correspond to the classification shown in Table 9, should be avoided due to their overall low reactivity. Another effect related to the tendency to overburn is the general decrease in the slaking T_{max} at higher burning temperatures (see

Figure 7c,d, and Tables 8 and 9). This fact is evident for all the samples, with the only significant exception of some dololimes (USI-10 and USI-10, see Figure 7c). In fact, these last samples showed an unusual increase in hydration temperature for limes burned at 1150 °C. This increase is mainly due to the latent and gradual reaction kinetics of the MgO component within the system, specifically the partial conversion of periclase to brucite [20].

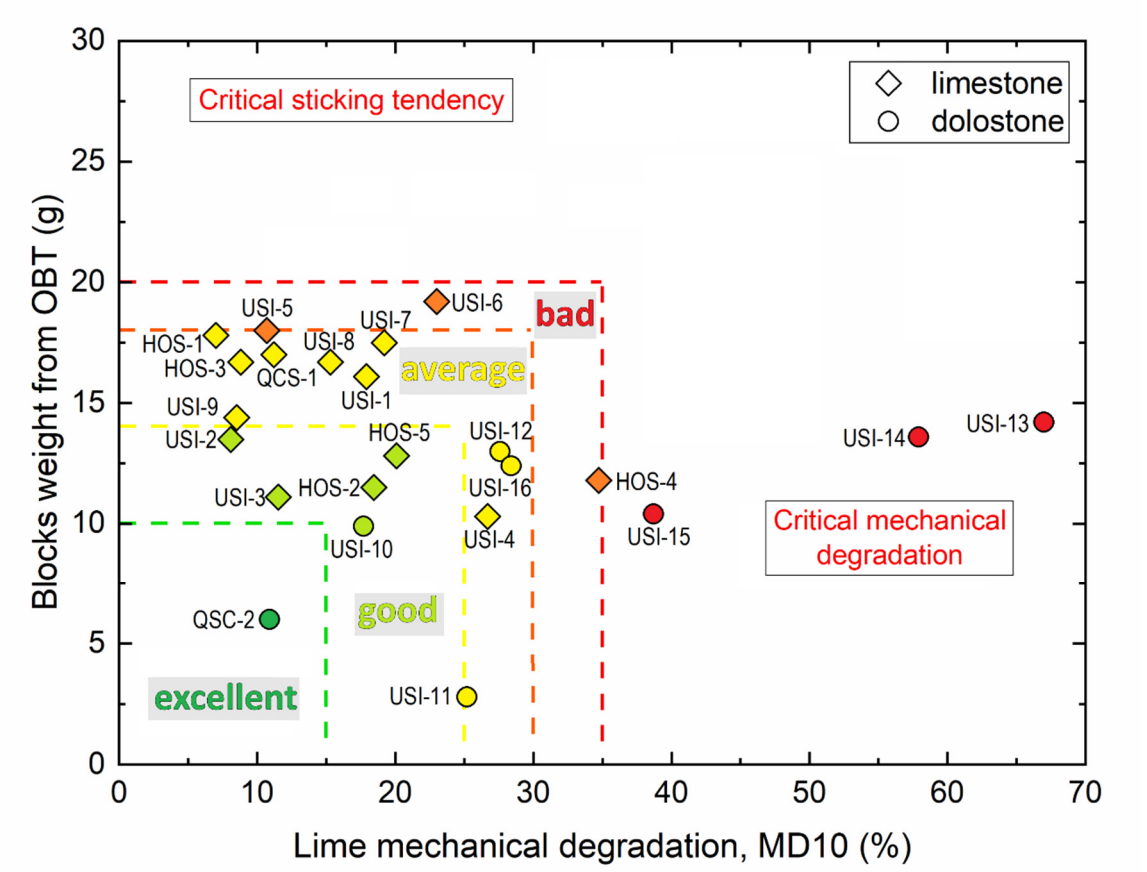


Figure 8. Empirical correlation between the Overburning Test (OBT) and fines passing 10 mm after the mechanical degradation (MD) test.

Incidentally, the classification given is essentially didactic, as it doesn't allow for unraveling possible correlations between slaking reactivity and various intrinsic geological characteristics of the parent rocks. Nevertheless, certain general trends can be observed. For instance, samples with high levels of impurities (insoluble residues) exhibit slower reactivity. In addition, samples from the UAE deposits considered in this study appear to be more reactive than samples from Iranian sites, with some notable exceptions. However, neither mineralogical-petrographic composition nor geological provenance can be used to predict the slaking reactivity of different raw materials. This fact, well-established in the literature [7–10] underlines that reactivity is a complex and unpredictable parameter that must always be determined experimentally. Furthermore, the above observations highlight the importance of constraining the performance of industrial kilns, particularly in terms of slaking reactivity, to specific raw materials sourced from known deposits. These raw materials should have a defined and potentially consistent mineralogical-petrographic composition with minimal impurities.

4.4. Mechanical Behavior and Sticking Tendency of the Lime

The MD at 10 mm for quicklime samples ranges between 7.0 and 34.9 wt%, with an average of 16.1 wt%. Conversely, the same parameter ranges between 10.9 and 67.0 wt%, with an average of 34.2 wt% for dololimes (see Table 8). Results clearly show that dololimes have a higher mechanical degradation or a lower mechanical behavior than quicklimes.

This agrees with previous data from the literature [14–16]. The sticking tendency (ST), determined by the OBT at 1300 °C, ranges between 10.3 and 19.2 g, with an average of 15 g, for quicklimes. Conversely, the ST for dololimes ranges from 2.8 to 14.2 g, with an average of 10.3 for dololimes (see Table 8). Results clearly show that quicklimes have a higher sticking tendency than dololimes, as already documented in the literature [11].

The formation of fine lime particles during the calcination process is a critical factor affecting the lime operation in industrial kilns. Therefore, the MD at 10 mm is considered one of the most reliable parameters for evaluating the efficiency of TSR kilns. At the same time, the same parameter is also useful for evaluating the suitability of raw materials for commissioning new plants. Moreover, from an industrial perspective, the possibility of predicting the degree of sticking tendency (ST) would also have a great impact on kiln design and operation. According to the mature scientific and industrial knowledge resulting from the analysis of the effects observed in dozens of plants worldwide, the formation of rings and blockages is considered more critical and frequent in the presence of an excess of fines that would be formed during the calcination process. Their occurrence essentially depends on the thermo-mechanical degradation processes of quicklime, which in turn are closely related to the textural-microstructural features of the parent carbonate rock [11]. Therefore, the empirical relationship between the Overburning Test (OBT) and Mechanical Degradation (MD) is shown in Figure 8. Acceptable ranges, critical limits, and practical solutions, as well as guidelines for kiln warranties, are discussed below. Each ST class is related to the expected residual CO_2 content of the burnt lime product, and additional suggestions are given to counteract fines excess (Table 3).

- Dark green field of "excellent" values (OBT < 10 g; MD < 15%): this field contains only one sample of dololime (QSC-2), which has extremely low MD and ST. This is the best sample in terms of physico-mechanical properties, behavior, and overburning tendency, making it suitable for TSR kilns at high temperatures using solid fuels. Therefore, the expectation for the residual CO_2, content will be very low (<1.0 wt%).
- Light green field of "good" values (OBT = 10–15 g; MD = 15–25%): this field concerns samples with low to medium ST and medium MD (HOS-2, HOS-5, USI-3, and USI-10). These samples have good physico-mechanical properties and combustion behavior, making them suitable for use in TSR kilns at HT using solid fuels. Therefore, the expectation for the residual CO_2 content will be low (<2.0 wt%).
- Yellow field of "average" values (OBT = 15–18 g; MD = 25–30%): this field concerns samples with medium to high ST coupled with medium to high MD (HOS-1, HOS-3, QSC-1, USI-1, USI-4, USI-7, USI-8, USI-9, USI-12, and USI-16). These samples have acceptable physico-mechanical properties and burning behavior and are therefore suitable for use in TSR kilns, but precautions must be taken. In particular, the use of a coarse fraction as kiln feed to counteract the production of fines is highly recommended. Moreover, the prevision for the residual CO_2 content will be high (2.0–3.0 wt%).
- Orange field of "bad" values (OBT = 18–20 g; MD = 30–35%): this field includes samples with high ST combined with high MD (HOS-4, USI-5, and USI-7). These samples are characterized by low physico-mechanical properties and low burning behavior, making them suitable for TSR kilns, but special precautions are required, especially for kilns using solid fuels. The use of a coarse fraction as kiln feed is strongly recommended. In addition, the expectation for the residual CO_2 content will be the highest (3.5–5.0 wt%).
- Red field of "critical" values (OBT > 20 g; MD > 35%): this field concerns samples with very high ST coupled with very high MD (USI-13, USI-14, and USI-15). These samples have critical physico-mechanical properties and are therefore generally not suitable for TSR kilns. No prevision can be given in terms of residual CO_2 content, and the customer is invited to change the raw material feeding the kiln.

5. Conclusions

This study focuses on industrial (air) lime production and utilizes an analytical database of 23 carbonate rocks from various high-grade deposits in the Arabian Peninsula and neighboring countries. Using an integrated microfacies analysis that includes mineralogical-petrographic analyses, micropaleontological investigations, and cathodoluminescence microscopy, we identified eight basic lithologies (four calcitic and four dolomitic types). The C-O-Sr isotopic signature also allowed the identification of at least ten different source deposits. In addition, carbon speciation and EPR spectroscopy were performed for comprehensive characterization.

The multi-analytical approach, previously used in the field of cultural heritage, has now been adapted for the first time to an industrial case study. This adaptation is crucial, as rock fabric, composition, stratigraphic age, and source deposits can all affect the quality of burnt lime products. These factors were carefully considered to impose additional constraints during kiln commissioning and the establishment of plant guarantees. In addition, a comprehensive technical characterization of the burnt limes produced was conducted to assess the suitability of the kilns for lime technologies. Performance prediction plays a key role in optimizing the process and ensuring quality control in TSR kilns.

Supplementary Materials: The following supporting information can be downloaded at: https://www.mdpi.com/article/10.3390/min13121500/s1. Table S1: TC400-ROC-TOC analyses on carbonate rocks. Values are the average of two different determinations. Symbols legend: TC400 = total carbon at 400 °C, ROC = residues oxidizable carbon at temperatures between 400 and 600 °C; TOC = total organic carbon; Dev.St = standard deviation of TOC values. Table S2: Results of the EPR spectral parameterisation. Values are referred to three different species in the spectra: Mn in (1) the calcic site in calcite (cc), (2) the magnesian site in dolomite (dol) (3) a pseudoisotropic site (3rd). The spread parameter was determined in all the species, whereas the spli and wav parameters were determined only in the prevailing species (cc or dol). The last column reports the categorical (presence/absence) information about the organic radical species. Symbol legend: ✔ = present. Figure S1: representative EPR spectra, registered at X-band and room temperature, highlighting all features described in the text: (a) typical pattern of Mn(II) in the Ca site in calcite; (b) spectrum arising from the superposition of a spectrum closely resembling that in (a) and another due to Mn(II) in the Mg site in dolomite; (c) spectrum arising from the superposition of the features due to Mn(II) in the Mg site in dolomite and those arising from Mn(II) in a third crystal chemical configuration; (d) spectrum of "calcitic" Mn(II) exhibiting, highlighted by the dashed ellipse, the signal due to the organic radical species. Table S3: The fundamental compositional and technical parameters of burnt lime products, including calcium oxide, magnesium oxide, slaking reactivity (referred as t_{50} or t_{60}) and residual CO_2 content [53–58].

Author Contributions: Conceptualization: G.V.; methodology: G.V., M.A., F.F., F.D.B., F.F. and C.N., data curation: G.V., M.A., G.F., F.D.B., F.F., F.L. and K.E.S.; formal analysis and investigation: G.V. and M.A.; writing—original draft preparation: G.V.; writing—review and editing: M.A., F.D.B., C.N., G.F., F.L., F.F. and K.E.S.; resources: G.V. and L.S.; supervision: L.S. and A.C. All authors have read and agreed to the published version of the manuscript.

Funding: This research received no external funding.

Data Availability Statement: Data is contained within the article or Supplementary Materials.

Acknowledgments: The authors would like to express their gratitude to the three anonymous reviewers and the Editor for their constructive suggestions and critical comments, which have contributed to the improvement of this paper.

Conflicts of Interest: The authors declare that they have no known competing financial interests or personal relationships that could have appeared to influence the work reported in this paper.

References

1. Beach, R.; Bullock, A.; Heller, K.; Domanico, J.L.; Muth, M.K.; O'Connor, A.C.; Spooner, R.B. *Lime Production: Industry Profile*; Final Report; Crump, E.L., Ed.; Research Triangle Institute: Research Triangle Park, NC, USA, 2000. Available online: https://www3.epa.gov/ttnecas1/regdata/IPs/Lime%2520Manufacturing_IP.pdf (accessed on 25 January 2023).

2. Boynton, R. *Chemistry and Technology of Lime and Limestone*; John Wiley & Sons: New York, NY, USA, 1980; pp. 311–315.
3. Oates, J. *Lime and Limestone. Chemistry and Technology, Production and Uses*; Wiley-VCH: Weinheim, Germany, 1998; p. 177.
4. Chang, L. *Industrial Mineralogy*; Pearson Education: Upper Saddle River, NJ, USA, 2002; pp. 101–191.
5. EuLA. *Innovation in the Lime Sector*; The European Lime Association: Bruxelles, Belgium, 2018; Available online: https://www.eula.eu/wp-content/uploads/2019/07/Innovation-in-the-Lime-Sector-.pdf (accessed on 25 January 2023).
6. Schorcht, F.; Kourti, I.; Scalet, B.M.; Roudier, S.; Sancho, L.D. *Best Available Techniques (BAT) Reference Document for the Production of Cement, Lime and Magnesium Oxide: Industrial Emissions Directive 2010/75/EU (Integrated Pollution Prevention and Control)*; EU Publications Office: Luxembourg, 2013; Available online: https://eippcb.jrc.ec.europa.eu/sites/default/files/2019-11/CLM_Published_def_0.pdf (accessed on 25 January 2023).
7. Vola, G. High-Grade Burnt Lime Products: Impact of Calcination Kinetics on Slaking Reactivity; Sticking Tendency and Blocks Formation at HT (1300 °C). Ph.D. Thesis, University of Ferrara, Ferrara, Italy, 2019; p. 282.
8. Vola, G.; Sarandrea, L.; Della Porta, G.; Cavallo, A.F.J.; Cruciani, G. The influence of petrography, mineralogy, and chemistry on burnability and reactivity of quicklime produced in Twin Shaft Regenerative (TSR) kilns from Neoarchean limestone (Transvaal Supergroup, South Africa). *Min. Pet.* **2018**, *112*, 555–576. [CrossRef]
9. Vola, G.; Bresciani, P.; Rodeghero, E.; Sarandrea, L.; Cruciani, G. Impact of rock fabric, thermal behavior, and carbonate decomposition kinetics on quicklime industrial production and slaking reactivity. *J. Therm. Anal. Calorim.* **2018**, *136*, 967–993. [CrossRef]
10. Vola, G.; Sarandrea, L.; Mazzieri, M.; Bresciani, P.; Ardit, M.; Cruciani, G. Reactivity and overburning tendency of quicklime burnt at high temperature. *ZKG Int.* **2019**, *10*, 20–31.
11. Vola, G.; Ardit, M.; Sarandrea, L.; Brignoli, G.; Natali, C.; Cavallo, A.; Bianchini, G.; Cruciani, G. Investigation and prediction of sticking tendency, blocks formation and occasional melting of lime at HT (1300 °C) by the Overburning Test method. *Constr. Build. Mater.* **2021**, *294*, 123577. [CrossRef]
12. Gosselin, C.; Verges-Belmin, V.; Royer, A.; Martinet, G. Natural cement and monumental restoration. *Mater. Struct.* **2009**, *42*, 749–763. [CrossRef]
13. Elsen, J.; Mertens, G.; Snellings, R. Portland cement and other calcareous hydraulic binders: History, production and mineralogy. In *Advances in the Characterization of Industrial Minerals*; EMU Notes in Mineralogy: London, UK, 2011; Volume 9, pp. 441–479.
14. Vola, G.; Christiansen, T.; Sarandrea, L.; Ferri, V. Carbonate rocks characterization for industrial lime manufacturing: Worldwide case-studies. In Proceedings of the EMABM 2013—14th Euroseminar on Microscopy Applied to Building Materials, Helsingør, Denmark, 10–14 June 2013.
15. Vola, G.; Sarandrea, L. Raw materials characterization for industrial lime manufacturing. *ZKG Int.* **2013**, *5*, 62–70.
16. Vola, G.; Sarandrea, L. Investigation and prediction of marble mechanical degradation and dust formation during calcination process in Twin Shaft Regenerative (TSR) kilns. *Cem. Int.* **2015**, *3*, 42–47.
17. Cwik, K.; Broström, M.; Backlund, K.; Fjäder, K.; Hiljanen, E.; Eriksson, M. Thermal Decrepitation and Thermally-Induced Cracking of Limestone Used in Quicklime Production. *Minerals* **2022**, *12*, 1197. [CrossRef]
18. EuLA. *A Pathway to Negative CO2 Emissions by 2050: The Contribution of the Lime Industry to a Carbon-Neutral Europe*; The European Lime Association: Brussels, Belgium, 2023; Available online: https://eula.eu/resources/a-pathway-to-negative-co2emissions-by-2050/ (accessed on 25 January 2023).
19. HaiDo, D.; Specht, E.; Kehse, G.; Ferri, V.; Christiansen, T.L.; Bresciani, P. Simulation of lime calcination in PFR kiln. Influence of energy input and lime throughput. *ZKG Int.* **2011**, *12*, 52–64.
20. Vola, G.; Massa, M.; Ardit, M.; Bresciani, P.; Sarandrea, L.; Cruciani, G. Process optimization and characterization of dolomitic hydrated limes with high BET specific surface area for "green" applications. In Proceedings of the SGI-SIMP-2022, Torino, Italy, 19–21 September 2022.
21. Manocha, S.; Ponchon, F. Management of Lime in Steel. *Metals* **2018**, *8*, 686. [CrossRef]
22. Conradt, R., II. 24—The industrial glass-melting process. In *The SGTE Casebook*, 2nd ed.; Series in Metals and Surface Engineering; Woodhead Publishing: Sawston, UK, 2008; pp. 282–303. [CrossRef]
23. Lesueur, D. Impact of quicklime reactivity and origin on Autoclaved Aerated Concrete production. *Cem. Wapno Beton* **2011**, *2011*, 16–21.
24. Sadik, C.; Moudden, O.; El BouariIz, A.; El Amrani, I. Review on the elaboration and characterization of ceramics refractories based on magnesite and dolomite. *J. Asian Ceram. Soc.* **2016**, *4*, 219–233. [CrossRef]
25. Al-Bashaireh, K. Ancient white marble trade and its provenance determination. *J. Archaeol. Sci. Rep.* **2021**, *35*, 102777. [CrossRef]
26. Antonelli, F.; Lazzarini, L. An updated petrographic and isotopic reference database for white marbles used in Antiquity. *Rend. Fis. Acc. Lincei* **2015**, *26*, 399–413. [CrossRef]
27. Lazzarini, L. Archaeometric aspects of white and coloured marbles used in antiquity: The state of the art. *Period. Mineral.* **2004**, *73*, 113–125.
28. Vola, G.; Ardit, M.; Frijia, G.; Cavallo, A.; Natali, C.; Mion, C.B.; Lugli, F.; Primavori, P. Characterization and provenance of historical-contemporaneous marbles from Waldensian valleys of Piedmont (Dora-Maira Massif, Cottian Alps, Italy). *J. Archaeol. Sci. Rep.* **2022**, *45*, 103562. [CrossRef]
29. African Geological Surveys. *Feuille N° 3: Carte Geologique de l'Afrique*; ASGA-UNESCO: Paris, France, 1963.
30. Munsell Color Co. *Munsell Rock Color Book with Genuine Munsell® Color Chips*; Munsell COLOR: Grand Rapids, MI, USA, 2009.

31. Flügel, E. *Microfacies of Carbonate Rocks: Analysis, Interpretation and Application*; Springer: Berlin/Heidelberg, Germany, 2010; p. 984.
32. Tucker, M.; Wright, W. *Carbonate Sedimentology*; Blackwell Science: Oxford, UK, 1990.
33. Scholle, P.; Ulmer-Scholle, D. *Color Guide to the Petrography of Carbonate Rocks: Grains, Textures, Porosity, Diagenesis*; AAPG Mem: Tulsa, OK, USA, 2003; Volume 77.
34. Dunham, R. *Classification of Carbonate Rocks According to Depositional Texture*; AAPG Mem: Tulsa, OK, USA, 1962; Volume 1, pp. 108–121.
35. Embry, A.; Klovan, J. A Late Devonian reef tract on Northeastern Banks Island. *Bull. Can. Petrol Geol.* **1971**, *19*, 730–781.
36. Wright, V. A revised classification of limestones. *Sediment. Geol.* **1992**, *76*, 177–185. [CrossRef]
37. Friedman, G. Terminology of recrystallization textures and fabrics in sedimentary rocks. *J. Sed. Petrol* **1965**, *35*, 643–655.
38. Sibley, D.; Gregg, J. Classification of dolomite rock textures. *J. Sed. Res.* **1987**, *57*, 967–975.
39. *UNI EN 459-1*; Building Lime. Part 1: Definitions, Specifications and Conformity Criteria. European Committee for Standardization: Brussels, Belgium, 2015. Available online: https://standards.iteh.ai/catalog/standards/cen/588081bb-ff4e-4421-997c-2d7dcab1b6ac/en-459-1-2015 (accessed on 25 January 2023).
40. Friedman, G. Identification of carbonate minerals by staining methods. *J. Sediment. Petrol.* **1959**, *29*, 87–97.
41. Rigaku. *Quantitative Analysis of Dolomite and Limestone by Pressed Powder Method with Supermini 200*; Rigaku Application note XRF 1058; Rigaku: Tokyo, Japan, 2015; p. 4. Available online: https://www.rigaku.com/newsletters/mabu/sept2018/app.note_xrf.pdf (accessed on 25 January 2023).
42. Moore, D.; Reynolds, R.J. X-ray Diffraction and the Identification and Analysis of Clay Minerals. *Clays Clay Miner.* **1997**, *38*, 448.
43. Cook, R. A comparison of methods for the extraction of smectites from calcareous rocks by acid dissolution techniques. *Clay Miner.* **1992**, *27*, 73–80. [CrossRef]
44. Bish, D.; Howard, S. Quantitative phase analysis using the Rietveld method. *J. Appl. Cryst.* **1988**, *21*, 86–91. [CrossRef]
45. Young, R. *The Rietveld Method. IUCr, Monograph on Crystallography*; Oxford University Press: Oxford, UK, 1993; p. 298.
46. Lugli, F.; Cipriani, A.; Peretto, C.; Mazzucchelli, M.; Brunelli, D. In situ high spatial resolution 87Sr/86Sr ratio determination of two Middle Pleistocene (ca 580 ka) *Stephanorhinus hundsheimensis* teeth by LA–MC–ICP–MS. *Int. J. Mass Spectrom.* **2017**, *412*, 38–48. [CrossRef]
47. McArthur, J.; Howarth, R.; Bailey, T. Strontium Isotope Stratigraphy: Lowess version 3: Best fit to the marine Sr-isotope curve for 0–509 Ma and accompanying look-up table for deriving numerical age. *J. Geol.* **2001**, *109*, 155–170. [CrossRef]
48. Zethof, J.; Leue, M.; Vogel, C.; Stoner, S.; Kalbitz, K. Identifying and quantifying geogenic organic carbon in soils—The case of graphite. *Soil* **2019**, *5*, 383–398. [CrossRef]
49. Natali, C.; Bianchini, G.; Carlino, P. Thermal stability of soil carbon pools: Inferences on soil nature and evolution. *Thermochim. Acta* **2019**, *683*, 178478. [CrossRef]
50. *UNI EN 459-2;* Building Lime—Part 2: Test Methods. European Committee for Standardization: Brussels, Belgium, 2021. Available online: https://standards.iteh.ai/catalog/standards/cen/7e034aed-a672-467a-8b6c-53c5d4f79a72/en-459-2-2010 (accessed on 25 January 2023).
51. Craig, H. Isotopic standards for carbon and oxygen and correction factors for mass-spectrometric analysis of carbon dioxide. *Geochim. Cosmochim. Acta* **1957**, *12*, 133–149. [CrossRef]
52. Alaabed, S.; Soltan, M.; Abdelghany, O.; Amin, B.; Tokhi, M.; Khaleel, A.; Musalim, A. United Arab Emirates limestones: Impact of petrography on thermal behaviour. *Mineral. Petrol.* **2014**, *108*, 837–852. [CrossRef]
53. Attanasio, D.; Brilli, M.; Ogle, N. *The Isotopic Signature of Classical Marbles*; L'Erma di Bretschneider: Rome, Italy, 2006; p. 297.
54. Romanelli, M.; Buccianti, A.; Di Benedetto, F.; Bellucci, L.; Cemicky, S. An innovative electron paramagnetic resonance and statistical analysis approach to investigate the geographical origin of multi-layered samples from a Renaissance painting. *Microchem. J.* **2022**, *177*, 107219. [CrossRef]
55. Piligkos, S.; Laursen, I.; Morgenstjerne, A.; Weihe, H. Sign and magnitude of Spin Hamiltonian parameters for Mn2+ impurities in calcite. A multi- and low-frequency EPR study. *Mol. Phys.* **2007**, *115*, 2025–2050. [CrossRef]
56. Vassilikou-Dova, A. EPR-determined site distributions of low concentrations of transition-metal ions in minerals: Review and predictions. *Am. Miner.* **1993**, *78*, 49–55.
57. Shepherd, R.; Graham, W. EPR of Mn^{2+} in polycrystalline dolomite. *J. Chem. Phys.* **1984**, *81*, 6080–6084. [CrossRef]
58. Reeder, R.; Markgraf, S. High-temperature crystal chemistry of dolomite. *Am. Miner.* **1986**, *71*, 795–804.

Disclaimer/Publisher's Note: The statements, opinions and data contained in all publications are solely those of the individual author(s) and contributor(s) and not of MDPI and/or the editor(s). MDPI and/or the editor(s) disclaim responsibility for any injury to people or property resulting from any ideas, methods, instructions or products referred to in the content.